J. Fluid Mech. (2003), *vol.* 477, *pp.* 89–128.
DOI: 10.1017/S0022112002003087 Printed in the United Kingdom

Green's functions for a source in a mixing layer: direct waves, refracted arrival waves and instability waves

By TAKAO SUZUKI† AND SANJIVA K. LELE

Department of Aeronautics and Astronautics, Stanford University, Stanford, CA 94305, USA

(Received 29 January 2001 and in revised form 28 August 2002)

Green's functions for a source embedded in an isothermal transversely sheared mixing layer are compared with direct numerical simulation (DNS) at various frequencies. Based on the third-order convective wave equation (Lilley 1974), three types of wave responses are analysed. For direct waves, a vortex sheet is used in the low-frequency limit, while in the high-frequency limit the procedure derived by Goldstein (1982) is re-visited. For refracted arrival waves propagating in the zone of silence, the vortex sheet model derived by Friedland & Pierce (1969) is re-visited in the low-frequency limit, while in the high-frequency limit the finite thickness model derived by Suzuki & Lele (2002) is applied. Instability waves excited by a very low-frequency source are formulated in the linear regime using the normal mode decomposition: eigen-functions are normalized using the adjoint convective wave equation, and the receptivity of instability waves is predicted. These theoretical predictions are compared with numerical simulations in two dimensions: DNS are performed based on the full Navier–Stokes equations (the free-stream Mach number is $M_1 = 0.8$, and the ratios of the acoustic wavelength to the vorticity thickness λ/δ_V are 4.0, 1.0 and 0.25). The DNS results agree fairly well with the high-frequency limit in all three cases for direct waves, although the lowest-frequency case ($\lambda/\delta_V = 4.0$) indicates some features predicted in the low-frequency limit. For refracted arrival waves, the DNS data follow the low- and high-frequency limits to a reasonable degree of accuracy in all cases. Moreover, by setting $\lambda/\delta_V = 16.0$, instability waves are simulated, and a comparison with the theoretical prediction shows that the instability wave response is predicted well when a mixing-layer Reynolds number is high ($Re = 10^5$). They also reveal that the receptivity is fairly sensitive to the Reynolds number and the source position within the mixing layer.

1. Introduction

In many aerodynamic flows, disturbances generated in a shear layer, such as instability waves, eddies, turbulence, etc. become potentially important noise sources (Lighthill 1952); thus, it is crucial to predict their sound radiation patterns in the far field. In general, the acoustic fields associated with a source embedded in transversely sheared flows are solved using the third-order convective wave equation with prescribed source terms. This wave equation, the so-called Lilley's equation (Lilley 1974; the original wave operator was derived by Pridmore-Brown 1958), can account

† Present address: California Institute of Technology, Division of Engineering and Applied Science, Pasadena, CA 91125, USA.

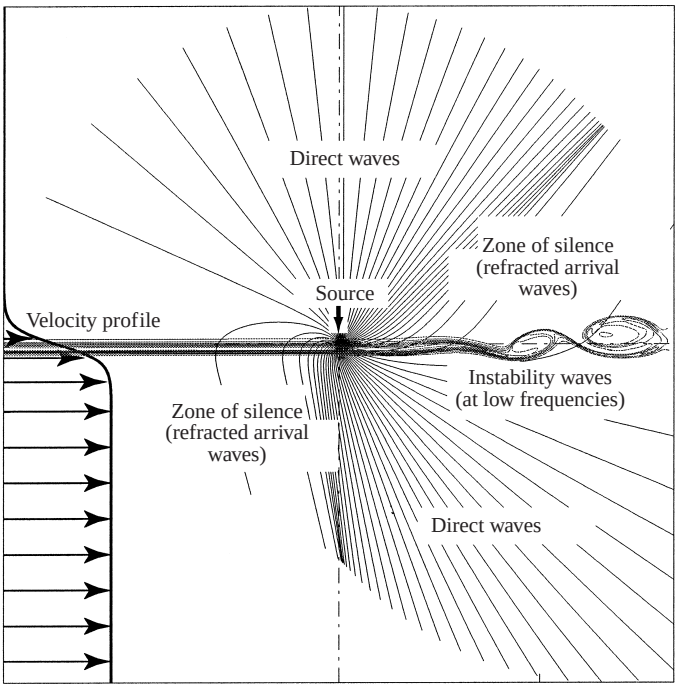

FIGURE 1. Schematic of a two-dimensional mixing layer. Typical ray trajectories of acoustic waves radiating from a point source are drawn. Vorticity contours associated with instability waves are overlapped.

for the refraction effect due to shear flows over the whole frequency range; hence, studies based on this equation are applicable to various aero-acoustic problems, such as jet noise, duct acoustics, sound from a turbulent boundary layer, etc. To develop a physical understanding of such acoustic problems, it is useful to formulate fundamental solutions which take into account refraction in a shear layer, namely Green's functions for the third-order convective wave equation. Green's functions for a source in a mixing layer are derived in this paper, and those in a boundary layer in Part 2 (Suzuki & Lele 2003), and these formulas are validated by using computational aero-acoustics (CAA).

When an acoustic source is embedded in a transversely sheared mixing layer, the emitted sound waves are refracted, and their radiation patterns are observed to be highly directional: adjacent to the directions of the peaked amplitude, there exist regions in which the sound level is fairly low, referred to as the zone of silence. As seen in figure 1, outside the zone of silence, acoustic waves can directly propagate and their wave fronts become circular. They are called 'direct waves'. By contrast, in the zone of silence, rays become very sparse and almost parallel. They are referred to as 'refracted arrival waves'. Waves of these two types determine the sound radiation pattern from a subsonic mixing layer. In addition to these sound waves, very low-frequency sources can excite 'instability waves', which grow exponentially with the downstream distance and could become secondary sound sources. For example, when the relative velocity of the instability wave disturbances is supersonic, they create Mach waves causing large sound in the zone of silence (Tam & Burton 1984). In this paper, three types of waves – direct waves, refracted arrival waves and instability waves – generated by a time-harmonic point source embedded in an isothermal transversely sheared mixing layer are investigated.

In previous studies, several asymptotic solutions for direct waves have been derived. In the application to jet noise, Mani (1976*a*, *b*) found analytical solutions for a point source embedded in a uniform jet. For more practical cases, particularly in the low-frequency limit, Goldstein (1975, 1976) and Balsa (1976) developed Green's functions for an axisymmetric transversely sheared flow. For a two-dimensional transversely sheared mixing layer, Goldstein (1978) studied the gust solutions, and this approach can be readily extended to sound waves. In these studies, the asymptotic solutions are obtained based on the third-order convective wave equation, and they are equivalent to the vortex sheet approximation. Approaches of this type are summarized by Beckemeyer (1974). In this paper, the low-frequency Green's functions for an arbitrary velocity profile of a transversely sheared flow are re-derived. These formulas are used to derive the low-frequency refracted arrival waves in the zone of silence. Moreover, the formula derived here can be readily extended for a moving source by simply changing the frame of reference.

Likewise, solutions to the high-frequency limit of direct waves have been studied by a number of researchers (Tester & Morfey 1976; Balsa 1976, 1977; Goldstein 1982; Durbin 1983*a*, *b*, and others). In particular, Goldstein (1982) explicitly derived Green's function in a two- and three-dimensional transversely sheared mixing layer by following the method developed by Avila & Keller (1963). In Goldstein's study, the convective wave equation is asymptotically solved using the stationary phase method in the far field. This derivation is reviewed in this paper. The acoustic fields of the low- and high-frequency asymptotic solutions show similar radiation patterns in the far field except near the zone of silence. However, the frequency range over which the low- or high-frequency limit remains accurate is still in question.

Another region in which the previous theories cannot adequately predict the sound level is the zone of silence. According to some previous studies, such as Tester & Morfey (1976), Balsa (1976), and Goldstein (1982), waves propagating in the zone of silence initially start as evanescent waves near the source. The amplitude is then exponentially damped before they penetrate the mixing layer. Consequently, the sound levels in the zone of silence are expected to be much smaller than the region in which direct rays are propagating. However, considerable sound levels have been measured in the zone of silence by experimental studies (Atvars, Schubert & Ribner 1965; Lush 1971; Tanna 1977). In fact, the computational results in the present study show that relatively strong plane waves are propagating in this region: instead of the primary waves being sufficiently suppressed in the mixing layer, plane waves leaking from the opposite side of the mixing layer become dominant in the zone of silence.

Plane waves of this type have been investigated in classical acoustic problems. They are sometimes called by different names: lateral waves (Landau & Lifshitz 1987), head waves (Keller & Lewis 1995), refracted arrival waves (Friedland & Pierce 1969; Howe 1970), and they are classified as diffracted waves. The approaches taken by these previous studies can be applied to refracted arrival waves at low frequencies in the current problem. These approaches can be categorized into two types: interface matching (Keller & Lewis 1995) and contour integral (Landau & Lifshitz 1987; Friedland & Pierce 1969; Howe 1970), leading to an identical result. In particular, Friedland & Pierce (1969) explicitly formulated refracted arrival waves for a line-source in a two-dimensional impinging jet using contour integrals. Howe (1970) also studied a similar case for a point source. However, the expressions are limited to the source located in the free stream. In this paper, the formulas of refracted arrival waves are extended for a source located at an arbitrary position inside the mixing layer using interface matching.

Although the formula obtained here gives the general plane wave form, the derivation follows the vortex sheet model, which is only valid when the acoustic wavelength is much longer than the vorticity thickness. In fact, the computational results in the current study demonstrate that at high frequencies the pressure amplitude becomes several times higher than the prediction based on the low-frequency limit. In a recent work, Suzuki & Lele (2002) showed that refracted arrival waves appear even at high frequencies and developed a formula for these waves based on geometrical acoustics. This theoretical study found that the far-field pressure amplitude is proportional to $\omega^{-1/2}\alpha^{-1}x^{-3/2}$ in the high-frequency limit, as opposed to $(\omega x)^{-3/2}$ in the low-frequency limit (where α is a parameter determined by the velocity profile and x denotes the distance from the source in the flow direction). The results of the current numerical study validate this theory.

The time-harmonic forced response of the mixing layer also contains instability waves. As the source frequency decreases, the wavenumber of the discrete solution crosses into the linearly unstable range. These waves are exponentially decaying in the vertical direction; hence, they do not propagate as sound in the far field. But, they are still solutions to the third-order convective wave equation in a compressible mixing layer. Several studies have investigated the receptivity of instability waves (Tam 1978; Balsa 1988, 1989). However, these studies assumed a piecewise smooth velocity profile and solved matching conditions at the interfaces. This paper describes a method to predict instability waves excited by a time-harmonic point source in an arbitrary velocity profile, which can be readily extended to sources of other types. This method is analogous to the one introduced in Part 2 (Suzuki & Lele 2003) to analyse channelled waves in a boundary layer, referred to as the normal mode decomposition (Ahluwalia & Keller 1977). Here, the acoustic field is expanded in a series of normal modes (eigenfunctions), and only the mode corresponding to the instability waves is extracted. To normalize the eigenfunction, the adjoint operator of the transformed convective wave equation and the corresponding 'inner product' are defined, which constitute the Hilbert space in this problem. This method is analogous to the viscous theory developed by Salwen & Grosch (1981) and modified to include the compressible inviscid theory for the current problem.

Thus, the objective of this study is to investigate Green's functions for a source embedded in a mixing layer over a wide frequency range. Here, Green's functions include direct waves and refracted arrival waves in both low- and high-frequency limits as well as instability waves. The flow is assumed to be an isothermal transversely sheared mixing layer. To investigate the intermediate frequency range, numerical simulations are performed in two dimensions: the full Navier–Stokes equations are solved by direct numerical simulation (DNS), and the numerical results are compared with the theoretical predictions. In these simulations, the free-stream Mach number is set to be $M_1 = 0.8$, and the ratios of the acoustic wavelength to the vorticity thickness are selected as $\lambda/\delta_V = 4.0$, 1.0, and 0.25 to investigate direct waves and refracted arrival waves. The computed pressure fields generated by a monopole-type source show that the $\lambda/\delta_V = 0.25$ and 1.0 cases agree well with the high-frequency asymptote for direct waves. Even the $\lambda/\delta_V = 4.0$ case is rather similar to the high-frequency limit, but it indicates some features predicted in the low-frequency limit. A comparison of refracted arrival waves shows that the DNS result at each frequency follows the corresponding frequency limit with a reasonable degree of accuracy: the $\lambda/\delta_V = 0.25$ case approaches the high-frequency limit, while the $\lambda/\delta_V = 4.0$ case is closer to the low-frequency limit. The series of DNS results also demonstrates that the relative strength of refracted arrival waves increases as the frequency becomes

higher. Note that their amplitude falls off as $x^{-3/2}$ toward downstream direction in two dimensions and x^{-2} in three dimensions, which are one order faster than those of direct waves, but the amplitude is maintained in the ray direction because these waves are general plane waves (in a two-dimensional sense). To investigate the receptivity of instability waves, a still lower frequency source ($\lambda/\delta_V = 16.0$) is simulated. The comparison between the theory and the DNS results shows good agreement when the Reynolds number is high ($Re = 10^5$). However, since the eigenmode of the adjoint wave equation has a very sharp peak, the inviscid theory is inadequate at the lower Reynolds number ($Re = 2.5 \times 10^3$). The results also reveal that the receptivity of instability waves is fairly sensitive to the source position within the mixing layer in the inviscid theory.

The outline of this paper is as follows. After the introduction, Green's functions for a source in a mixing layer are formulated in § 2: both low- and high-frequency asymptotes of direct waves and refracted arrival waves are derived; also, the method to predict instability waves is described. In § 3, the procedures of the numerical simulations are described. In § 4, the theoretical predictions and the numerical results are compared and discussed. In the last section, conclusions are presented.

2. Derivation of Green's functions

When the acoustic wavelength is much longer than the length scale over which the medium varies (the vorticity thickness of the mixing layer in this case), one can assume a low-frequency limit. To be precise, one should call it a 'long wavelength limit' but in this paper only the term 'low-frequency limit' (or 'high-frequency limit' for the opposite limit) is used according to the general convention. In this section, the low- and high-frequency limits of direct waves and refracted arrival waves are derived. These formulas revisit or extend previous studies. In addition to these two types of sound waves, a method to predict instability waves excited by a time-harmonic point source is successfully developed. This method is applicable to any frequency range and an arbitrary velocity profile. Using this method, the receptivity of instability waves can be simply calculated as a function of the source position.

2.1. *Low-frequency Green's function for direct waves*

One can start with the linearized homogeneous third-order convective wave equation (for its derivation, refer to Pridmore-Brown 1958 or Lilley 1974):

$$\frac{\mathrm{D}}{\mathrm{D}t}\left[\frac{\mathrm{D}^2\Pi}{\mathrm{D}t^2} - \frac{\partial}{\partial x_j}\left(a^2\frac{\partial \Pi}{\partial x_j}\right)\right] + 2\frac{\partial u_k}{\partial x_j}\frac{\partial}{\partial x_k}\left(a^2\frac{\partial \Pi}{\partial x_j}\right) = 0, \tag{2.1}$$

where $\mathrm{D}/\mathrm{D}t \equiv \partial/\partial t + u_j\partial/\partial x_j$ and $\Pi \equiv \gamma^{-1}\log(p/p_\infty)$ (γ denotes the specific heat ratio and p_∞ the ambient pressure). The following characteristic scales are used to non-dimensionalize the equations: the speed of sound a_∞ is taken to be the velocity scale, and the ambient acoustic wavelength λ to be the length scale; hence, the time scale is normalized by λ/a_∞. Note that the angular frequency should be replaced by 2π, but the symbol ω is retained in this paper for convenience. In the low-frequency limit, a characteristic length of the mixing layer ϵ, which is non-dimensionalized by the acoustic wavelength, is much smaller than unity. A precise definition of ϵ is given later, but its order is equivalent to that of the vorticity thickness. All quantities are non-dimensionalized based on these scales, unless otherwise noted.

Assume that the mean velocity is only vertically sheared in two dimensions, namely $M(y)$ (M denotes the Mach number in a non-dimensional form). Here, the x coordi-

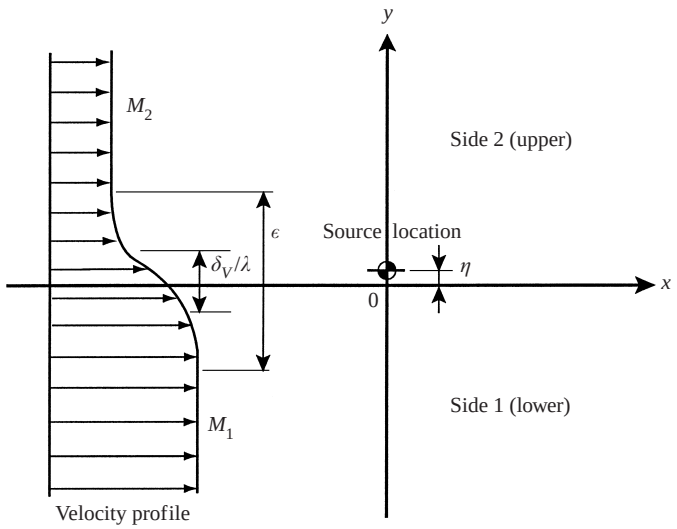

FIGURE 2. Coordinate system of a two-dimensional mixing layer.

nate is taken to be the mean flow direction, y to be the vertical direction, and z to be the spanwise direction (see figure 2). Moreover, assume that the mean temperature variation is negligible. Recall that when the free-stream temperatures are equal on both sides, the Crocco–Busemann relation gives the maximum temperature variation as $\frac{1}{2}(\gamma-1)M^2(1-M^2)$ in a mixing layer (which is less than 13% if $M < 1.2$ for $\gamma = 1.4$). After taking a Fourier transform of (2.1) in time and the flow direction x, it yields

$$\frac{\partial^2 \hat{\Pi}}{\partial y^2} + \frac{2k\mathrm{d}M/\mathrm{d}y}{\omega - kM}\frac{\partial \hat{\Pi}}{\partial y} + [(\omega - kM)^2 - k^2]\hat{\Pi} = 0, \tag{2.2}$$

where

$$\hat{\Pi}(\omega, k, y) = \frac{1}{(2\pi)^2}\int_{-\infty}^{\infty}\int_{-\infty}^{\infty} \Pi(t, x, y)\,\mathrm{e}^{\mathrm{i}\omega t}\mathrm{e}^{-\mathrm{i}kx}\mathrm{d}t\,\mathrm{d}x. \tag{2.3}$$

Now, consider Green's function for the transformed convective wave operator (2.2), i.e. solve the following equation:

$$\frac{\partial^2 \hat{G}_{(1)}}{\partial y^2} - 2\frac{\bar{n}'}{\bar{n}}\frac{\partial \hat{G}_{(1)}}{\partial y} + \omega^2(\bar{n}^2 - \bar{k}^2)\hat{G}_{(1)} = \delta(y - \eta), \tag{2.4}$$

where $\bar{n}(y) \equiv 1 - \bar{k}M(y)$, which corresponds to an 'index of refraction', and $\bar{k}$ is the normalized wavenumber in the x-direction. They are defined by $n = \omega\bar{n}$ and $k = \omega\bar{k}$, respectively. In addition, η denotes the source position, and the subscript (1) denotes the dimension. Here, one-dimension (1) refers to the solution in the (ω, k) domain or for plane waves. To estimate the order of each term in (2.4), define ϵ to be several times larger than the vorticity thickness so that it satisfies

$$\left|\frac{M(+\infty) - M(\epsilon)}{M(+\infty) - M(-\infty)}\right| \ll 1 \quad \text{and} \quad \left|\frac{M(-\epsilon) - M(-\infty)}{M(+\infty) - M(-\infty)}\right| \ll 1.$$

Yet ϵ is much smaller than the acoustic wavelength, namely $\epsilon \ll 1$ (see figure 2).

To obtain the low-frequency asymptotic Green's function, solutions in the inner and outer regions are solved separately and are matched at $y = \pm\epsilon$. The asymptotic

matching described in Appendix A provides the following solution for plane waves:

$$\hat{G}_{(1)}^{DR,low}(y) = \frac{\exp\left[\mathrm{i}\left(\mp\omega\sqrt{\bar{n}_J^2 - \bar{k}^2}\,y - \dfrac{\pi}{2}\right)\right]}{\omega\bar{n}_\eta^2\left(\dfrac{\sqrt{\bar{n}_2^2 - \bar{k}^2}}{\bar{n}_2^2} + \dfrac{\sqrt{\bar{n}_1^2 - \bar{k}^2}}{\bar{n}_1^2}\right)}, \quad \begin{cases} y \leqslant -\epsilon : & J = 1 \\ y \geqslant \epsilon : & J = 2. \end{cases} \tag{2.5}$$

Here, the superscripts '*DR*' and '*low*' represent the solution for direct waves and the low-frequency limit, respectively. The subscript $J = 1$ denotes the lower side, $J = 2$ the upper side, and $\bar{n}_\eta \equiv \bar{n}(y = \eta)$. If $y \leqslant -\epsilon$, the minus sign is taken inside the exponential, while for $y \geqslant +\epsilon$ the plus sign is taken. This notation is applied throughout this paper. At the leading order, the amplitudes on both sides are the same and the solution only depends on the velocity at the source position via $\bar{n}_\eta$ in the far field. Note that the expression (2.5) remains valid even when the wave becomes evanescent.

Next, derive Green's function for a line source (two dimensions), namely the solution to the following equation:

$$\frac{\mathrm{D}}{\mathrm{D}t}\left[\frac{\mathrm{D}^2 G}{\mathrm{D}t^2} - \frac{\partial}{\partial x_j}\left(a^2\frac{\partial G}{\partial x_j}\right)\right] + 2\frac{\partial u_k}{\partial x_j}\frac{\partial}{\partial x_k}\left(a^2\frac{\partial G}{\partial x_j}\right) = \frac{\mathrm{D}}{\mathrm{D}t}[\mathrm{e}^{-\mathrm{i}\omega t}\delta(x)\delta(y-\eta)]. \tag{2.6}$$

Setting the source term as shown above, the limit of $M \to 0$ yields the solution to the regular monopole which one would naturally expect rather than just setting $\mathrm{e}^{-\mathrm{i}\omega t}\delta(x)\delta(y-\eta)$. Now, the two-dimensional solution can be derived by simply taking an inverse Fourier transform of (2.5),

$$\hat{G}_{(2)}(x, y \mid \omega, 0, \eta) = \frac{1}{2\pi\mathrm{i}}\int_{-\infty}^{\infty} \frac{\exp\left[\mathrm{i}\omega\left(\bar{k}_x x \mp \sqrt{\bar{n}_J^2 - \bar{k}_x^2}\,y\right)\right]}{\bar{n}_\eta^2\left(\dfrac{\sqrt{\bar{n}_2^2 - \bar{k}_x^2}}{\bar{n}_2^2} + \dfrac{\sqrt{\bar{n}_1^2 - \bar{k}_x^2}}{\bar{n}_1^2}\right)}\,\mathrm{d}\bar{k}_x. \tag{2.7}$$

Here, the arguments of $\hat{G}$ before the vertical bar denote the observer position, and the ones after denote the source frequency and the source position. This is the low-frequency Green's function in two dimensions where a delta function is located at $(0, \eta)$, and the expression is valid in both near and far fields.

In studies of noise radiation, the far-field representation is of general interest. In such a case, an asymptotic solution of (2.7) can be derived in an explicit form. Define $x \equiv r\cos\phi$ and $y \equiv r\sin\phi$ ($r \gg 1$), and use the stationary phase method. On the lower side ($J = 1$), the phase part can be expressed by $\varphi(\bar{k}_x) = \bar{k}_x\cos\phi - \sqrt{\bar{n}_1^2 - \bar{k}_x^2}\sin\phi$, and its first derivative becomes zero when

$$\bar{k}_x^\star = \frac{1}{1 - M_1^2}\left(-M_1 + \frac{\cos\phi}{\sqrt{1 - M_1^2\sin^2\phi}}\right), \tag{2.8}$$

which is usually referred to as a stationary point, represented by the superscript $\star$. Note that in supersonic flows ($M_1 > 1$), (2.8) is valid only where $\phi < \arcsin(1/M_1)$, namely within a Mach cone. Since the second derivative of the phase part becomes $\varphi''(\bar{k}_x^\star) = -(1 - M_1^2\sin^2\phi)^{3/2}/\sin^2\phi$ (< 0), the asymptotic far-field solution on the

lower side yields

$$\hat{G}^{DR,low}_{(2)}(r,\phi \mid \omega,0,\eta) \approx \frac{|\sin\phi|}{\sqrt{2\pi\omega r}(1-M_1^2\sin^2\phi)^{3/4}} \frac{\exp\left[\mathrm{i}\left(\dfrac{-M_1\cos\phi+\sqrt{1-M_1^2\sin^2\phi}}{1-M_1^2}\omega r-\frac{3}{4}\pi\right)\right]}{(\bar{n}^\star_\eta)^2\left(\dfrac{\sqrt{(\bar{n}^\star_2)^2-(\bar{k}^\star_x)^2}}{(\bar{n}^\star_2)^2}+\dfrac{\sqrt{(\bar{n}^\star_1)^2-(\bar{k}^\star_x)^2}}{(\bar{n}^\star_1)^2}\right)} \quad (y<0 \text{ and } r\to\infty), \tag{2.9}$$

where the superscript $\star$ denotes a quantity evaluated at $\bar{k}_x=\bar{k}^\star_x$. The expression corresponding to (2.9) on the upper side ($J=2$) can be obtained by just swapping the subscripts 1 and 2. Notice that the amplitude becomes peaked near $(\bar{n}^\star_J)^2-(\bar{k}^\star_x)^2=0$ ($J=1,2$), which is different from the peak in the high-frequency limit (refer to Appendix B for a discussion of the peak angles and see (2.18) later for the high-frequency limit). In the low-frequency limit, direct waves can even propagate beyond the peak angles in theory; however, refracted arrival waves become dominant in these regions in reality. Later, (2.9) will be used to derive the expression for the low-frequency refracted arrival waves.

The three-dimensional solution for a point source can be derived in the same manner. Only the results are shown here. The general expression is

$$\hat{G}^{DR,low}_{(3)}(x,y,z \mid \omega,0,\eta,0)=\frac{\omega}{(2\pi)^2\mathrm{i}}\iint_{-\infty}^{\infty}\frac{\exp\left[\mathrm{i}\omega\left(\bar{k}_x x\mp\sqrt{\bar{n}_J^2-\bar{k}_x^2-\bar{k}_z^2}\,y+\bar{k}_z z\right)\right]}{\bar{n}_\eta^2\left(\dfrac{\sqrt{\bar{n}_2^2-\bar{k}_x^2-\bar{k}_z^2}}{\bar{n}_2^2}+\dfrac{\sqrt{\bar{n}_1^2-\bar{k}_x^2-\bar{k}_z^2}}{\bar{n}_1^2}\right)}\,\mathrm{d}\bar{k}_x\,\mathrm{d}\bar{k}_z. \tag{2.10}$$

Defining $x\equiv r\sin\theta\cos\phi$, $y\equiv r\sin\theta\sin\phi$, and $z\equiv r\cos\theta$, the stationary point becomes

$$\bar{k}^\star_x=\frac{1}{1-M_J^2}\left[-M_J+\frac{\sin\theta\cos\phi}{\sqrt{1-M_J^2(\cos^2\theta+\sin^2\theta\sin^2\phi)}}\right], \tag{2.11}$$

$$\bar{k}^\star_z=\frac{\cos\theta}{\sqrt{1-M_J^2(\cos^2\theta+\sin^2\theta\sin^2\phi)}}. \tag{2.12}$$

Thus, the far-field solution yields

$$\hat{G}^{DR,low}_{(3)}(r,\theta,\phi \mid \omega,0,\eta,0) \approx \frac{-1}{2\pi r}\frac{\sin\theta|\sin\phi|}{1-M_J^2(\cos^2\theta+\sin^2\theta\sin^2\phi)} \times\frac{\exp\left[\mathrm{i}\dfrac{-M_J\sin\theta\cos\phi+\sqrt{1-M_J^2(\cos^2\theta+\sin^2\theta\sin^2\phi)}}{1-M_J^2}\omega r\right]}{(\bar{n}^\star_\eta)^2\left(\dfrac{\sqrt{(\bar{n}^\star_2)^2-(\bar{k}^\star_x)^2-(\bar{k}^\star_z)^2}}{(\bar{n}^\star_2)^2}+\dfrac{\sqrt{(\bar{n}^\star_1)^2-(\bar{k}^\star_x)^2-(\bar{k}^\star_z)^2}}{(\bar{n}^\star_1)^2}\right)}. \tag{2.13}$$

This completes the derivation of the low-frequency Green's functions for direct waves in a mixing layer with an arbitrary velocity profile.

2.2. *High-frequency Green's function for direct waves*

One can apply a similar procedure to derive Green's function in the high-frequency limit. Start with (2.4), and convert its dependent variable by defining $\hat{G}^{\bullet}_{(1)} \equiv \hat{G}_{(1)}/(1-\bar{k}M(y))$; consequently, (2.4) can be rewritten as

$$\frac{\partial^2 \hat{G}^{\bullet}_{(1)}}{\partial y^2} + \omega^2 \left[\bar{n}^2 - \bar{k}^2 - \frac{\bar{n}}{\omega^2}\frac{\partial^2}{\partial y^2}\left(\frac{1}{\bar{n}}\right)\right]\hat{G}^{\bullet}_{(1)} = \frac{\delta(y-\eta)}{\bar{n}}. \tag{2.14}$$

Notice that the second derivative term $(\bar{n}/\omega^2)(\partial^2/\partial y^2)(1/\bar{n})$ is negligible at high-frequencies. Note also that since ω is equal to 2π in this paper, $\bar{n}/\omega^2$ does not become small, but $(\partial^2/\partial y^2)(1/\bar{n})$ does. Following the procedure derived by Avila & Keller (1963) (see Appendix C), the solution to (2.14) yields

$$\hat{G}^{DR,high}_{(1)}(y) = \frac{\bar{n}_2 \exp\left[\mathrm{i}\omega \int_{\eta}^{y} \sqrt{\bar{n}(y')^2 - \bar{k}^2}\,\mathrm{d}y'\right]}{\mathrm{i}2\omega\bar{n}_{\eta}(\bar{n}_{\eta}^2 - \bar{k}^2)^{1/4}(\bar{n}_2^2 - \bar{k}^2)^{1/4}}. \tag{2.15}$$

Here again, the superscript '*high*' represents the high-frequency limit. Unlike the low-frequency limit, the amplitude on each side is independent of the velocity profile on the other side. One can easily deduce this result from the fact that reflected waves are negligible in the high-frequency limit.

On taking an inverse Fourier transform to obtain a line source solution, the phase part becomes $\varphi(\bar{k}_x) = (\bar{k}_x x + \int_{\eta}^{y} \sqrt{\bar{n}(y')^2 - \bar{k}_x^2}\,\mathrm{d}y')/r$, from which the stationary point $\varphi'(\bar{k}_x) = 0$ cannot be explicitly solved. However, when the distance between the mixing layer and the observer point is much larger than the vorticity thickness ($r \gg \epsilon$) as well as the wavelength ($r \gg 1$), the phase part can be evaluated as follows:

$$\begin{aligned}\varphi(\bar{k}_x) &= \frac{1}{r}\left[\bar{k}_x x + \int_0^y \sqrt{\bar{n}^2(y) - \bar{k}_x^2}\,\mathrm{d}y' - \int_0^y \left(\sqrt{\bar{n}^2(y) - \bar{k}_x^2} - \sqrt{\bar{n}^2(y') - \bar{k}_x^2}\right)\mathrm{d}y'\right. \\ &\quad \left. - \int_0^{\eta} \sqrt{\bar{n}^2(y') - \bar{k}_x^2}\,\mathrm{d}y'\right] \\ &= \bar{k}_x \cos\phi + \sqrt{\bar{n}(y)^2 - \bar{k}_x^2}\sin\phi + O(\epsilon/r).\end{aligned} \tag{2.16}$$

Here, notice that the term $\sqrt{\bar{n}^2(y) - \bar{k}_x^2} - \sqrt{\bar{n}^2(y') - \bar{k}_x^2}$ becomes non-zero only in $0 < y < \epsilon$. Thus, the stationary point can be approximated by the same expression as derived in the low-frequency limit,

$$\bar{k}_x = \frac{1}{1-M_J^2}\left(-M_J + \frac{\cos\phi}{\sqrt{1 - M_J^2\sin^2\phi}}\right) + O(\epsilon/r) \equiv \bar{k}_x^{\star} + \delta\bar{k}_x. \tag{2.17}$$

While (2.17) can be substituted to evaluate the amplitude part, it cannot be used for the phase part. In the phase part the error becomes of the order of $\omega r \times O(\epsilon/r) = O(\epsilon)$, which is much greater than unity in the high-frequency limit. Consequently, using the

stationary phase method, the result can be expressed as

$$\hat{G}^{DR,high}_{(2)}(r,\phi \mid \omega,0,\eta)$$
$$\approx \frac{1}{2\sqrt{2\pi\omega r}}\frac{\sqrt{\sin\phi}\left(\sqrt{1-M_J^2\sin^2\phi}-M_J\cos\phi\right)\exp\left[\mathrm{i}\left(\omega r\varphi(\bar{k}_x^\star+\delta\bar{k}_x)-\tfrac{3}{4}\pi\right)\right]}{(1-M_J^2)(1-M_J^2\sin^2\phi)\bar{n}_\eta^\star((\bar{n}_\eta^\star)^2-(\bar{k}_x^\star)^2)^{1/4}}, \tag{2.18}$$

where $\bar{n}_\eta^\star = 1-\bar{k}_x^\star M_\eta$. Thus, the amplitude becomes peaked when $(\bar{n}_\eta^\star)^2-(\bar{k}_x^\star)^2=0$, beyond which acoustic rays cannot propagate, referred to as the 'zone of silence' (see Appendix B). Likewise, the three-dimensional case can be derived as follows:

$$\hat{G}^{DR,high}_{(3)}(r,\theta,\phi \mid \omega,0,\eta,0)$$
$$\approx \frac{-1}{4\pi r}\frac{\sqrt{\sin\theta|\sin\phi|}\left[\sqrt{1-M_J^2(\cos^2\theta+\sin^2\theta\sin^2\phi)}-M_J\sin\theta\cos\phi\right]}{(1-M_J^2)\left[1-M_J^2(\cos^2\theta+\sin^2\theta\sin^2\phi)\right]^{5/4}}$$
$$\times\frac{\exp[\mathrm{i}\omega r\varphi(\bar{k}_x^\star+\delta\bar{k}_x,\bar{k}_z^\star+\delta\bar{k}_z)]}{\bar{n}_\eta^\star((\bar{n}_\eta^\star)^2-(\bar{k}_x^\star)^2-(\bar{k}_z^\star)^2)^{1/4}}. \tag{2.19}$$

Here, the leading terms of $\bar{k}_x^\star$ and $\bar{k}_z^\star$ are given by (2.11) and (2.12), respectively.

2.3. *Low-frequency Green's function for refracted arrival waves*

Supposing that $M_1 > M_2$ and a point source is located beneath a mixing layer (see figure 2 again), then there exist regions on the upper side downstream and the lower side upstream which direct waves cannot reach, referred to as the zone (or cone) of silence. Friedland & Pierce (1969) proved that general plane waves, called refracted arrival waves (or often called lateral waves, head waves, and so on), propagate in the zone of silence: instead of direct waves being evanescent, the disturbances on the opposite side of the mixing layer invoke sound waves. The same phenomenon occurs even when the source is located inside the mixing layer. To formulate such refracted arrival waves at low frequencies, two approaches can be considered. One is to start with the integral form of the low-frequency Green's function described in § 2.1 and to calculate a contour integral in taking an inverse Fourier transform. The other approach, which is described in this section, uses the matching condition at the interface. This method is more intuitive from a physical point of view. Both approaches lead to an identical result.

Consider a two-dimensional mixing layer ($M_1 > M_2$), and start with the low-frequency Green's function (2.9). Referring to (2.8), the wavenumber in the x-direction just beneath the mixing layer becomes

$$\bar{k}_x^\diamond \equiv \frac{1}{1+M_1}. \tag{2.20}$$

Now, the disturbance with $\bar{k}^\diamond$ generates plane waves in the zone of silence on the upper side. Hence, the solution on the upper side can be expressed in the following form:

$$\hat{G}^{RF,low}_{(2)}(x,y \mid \omega,0,\eta) = \mathscr{A}(x-\frac{y}{\tan\phi^\diamond})\exp\left[\mathrm{i}\omega\left(\bar{k}_x^\diamond x+\sqrt{(\bar{n}_2^\diamond)^2-(\bar{k}_x^\diamond)^2}\,y\right)\right], \tag{2.21}$$

where the superscript '*RF*' represents the solution for refracted arrival waves and

$\bar{n}_2^\diamond \equiv 1 - \bar{k}^\diamond M_2$. Here, $\phi^\diamond$ is the ray direction of refracted arrival waves defined by

$$\bar{k}_x^\diamond = \frac{1}{1-M_2^2}\left(-M_2 + \frac{\cos\phi^\diamond}{\sqrt{1-M_2^2\sin^2\phi^\diamond}}\right). \tag{2.22}$$

For two-dimensional plane waves, the amplitude is conserved along the ray direction (which is not identical to the direction normal to the wave front, in general); hence, it can be determined only by the initial position within the mixing layer (defined by X) at which the ray starts.

The solution on the upper side (2.21) and that on the lower side (2.9) must satisfy the jump conditions across the mixing later, which determine the amplitude $\mathscr{A}(X)$. As shown in Appendix A, a pair of jump conditions, (A 9) and (A 10), must be imposed across the vortex sheet. However, the continuity (A 9) is automatically adjusted by waves which are propagating just beneath the mixing layer and eventually appear as refracted arrival waves. Therefore, the only remaining jump condition, the derivative matching (A 10), must be satisfied as

$$\left.\frac{1}{(\bar{n}_1^\diamond)^2}\frac{\partial \hat{G}_{(2)}^{DR,low}}{\partial y}\right|_{-\epsilon} = \left.\frac{1}{(\bar{n}_2^\diamond)^2}\frac{\partial \hat{G}_{(2)}^{RF,low}}{\partial y}\right|_{+\epsilon}. \tag{2.23}$$

This yields the formula for refracted arrival waves in the low-frequency limit given as follows (refer to Suzuki 2001 for the detailed algebraic procedure):

$$\hat{G}_{(2)}^{RF,low}(r,\phi \mid \omega,0,\eta) \approx \frac{1}{\sqrt{2\pi}(\omega r)^{3/2}\left(\cos\phi - \dfrac{\sin\phi}{\tan\phi^\diamond}\right)^{3/2}}\frac{(\bar{n}_2^\diamond)^4}{(\bar{n}_1^\diamond)^2(\bar{n}_\eta^\diamond)^2} \times \frac{\exp\left[\mathrm{i}\left(\bar{k}^\diamond\cos\phi + \sqrt{(\bar{n}_2^\diamond)^2-(\bar{k}_x^\diamond)^2}\sin\phi\right)\omega r - \mathrm{i}\pi/4\right]}{(\bar{n}_2^\diamond)^2-(\bar{k}_x^\diamond)^2}. \tag{2.24}$$

The expression for refracted arrival waves on the lower side can be similarly derived by swapping the subscripts 1 and 2. This derivation provides an intuitive sense that the disturbances on one side cause refracted arrival waves on the other side. It should be emphasized that the amplitude falls off as $r^{-3/2}$ in the x-direction; however, since the form of the solution is general plane waves, its amplitude is constant in the ray direction.

Refracted arrival waves in three dimensions could be similarly derived by retaining $\bar{k}_z$ and taking an inverse Fourier transform with respect to $\bar{k}_z$. In fact, this process can be accomplished using the stationary phase method in the z-direction; however, this derivation becomes algebraically complicated. Instead, a more physically understandable derivation is possible using the ray tube theory. The comparison between the ray tube theory and the inverse Fourier transform will be used later to derive refracted arrival wave at high-frequencies in § 2.4.

First, consider the upper half-space, and define the point at which refracted arrival waves arise in the mixing layer as $(X,0,Z) = (R\sin\Theta, 0, R\cos\Theta)$. Refer to figure 3 for a schematic. The wavenumber at the zenithal angle Θ can be obtained from (2.11)

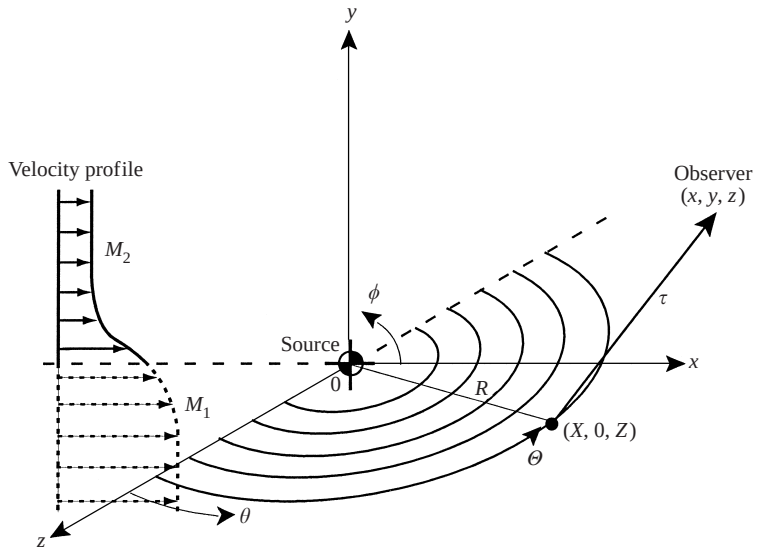

FIGURE 3. Coordinate system for refracted arrival waves in three dimensions.

and (2.12) as

$$\bar{k}_x^\diamond = \frac{1}{1-M_1^2}\left(-M_1 + \frac{\sin\Theta}{\sqrt{1-M_1^2\cos^2\Theta}}\right), \tag{2.25}$$

$$\bar{k}_z^\diamond = \frac{\cos\Theta}{\sqrt{1-M_1^2\cos^2\Theta}}. \tag{2.26}$$

From the point $(X,0,Z)$, a ray radiates in the following direction:

$$\dot{x}^\diamond(\bar{k}_x^\diamond,\bar{k}_z^\diamond) \equiv \frac{\mathrm{d}x}{\mathrm{d}\tau} = \frac{\bar{k}_x^\diamond}{\bar{n}_2^\diamond} + M_2, \tag{2.27}$$

$$\dot{y}^\diamond(\bar{k}_x^\diamond,\bar{k}_z^\diamond) \equiv \frac{\mathrm{d}y}{\mathrm{d}\tau} = \frac{\sqrt{(\bar{n}_2^\diamond)^2-(\bar{k}_x^\diamond)^2-(\bar{k}_z^\diamond)^2}}{\bar{n}_2^\diamond}, \tag{2.28}$$

$$\dot{z}^\diamond(\bar{k}_x^\diamond,\bar{k}_z^\diamond) \equiv \frac{\mathrm{d}z}{\mathrm{d}\tau} = \frac{\bar{k}_z^\diamond}{\bar{n}_2^\diamond}. \tag{2.29}$$

Here, τ denotes the non-dimensional characteristic time scale. These formulas can be readily derived from geometrical acoustics (e.g. Keller & Lewis 1995; Pierce 1989). Combining these expressions, an arbitrary point in the zone of silence can be represented by $(x,y,z) = (R\sin\Theta + \dot{x}^\diamond\tau, \dot{y}^\diamond\tau, R\cos\Theta + \dot{z}^\diamond\tau)$.

Next, consider the change of the area ratio by calculating the Jacobian. The unit area at an arbitrary point in the zone of silence can be computed as follows:

$$\left(\frac{\partial \boldsymbol{x}}{\partial R}\times\frac{\partial \boldsymbol{x}}{\partial\Theta}\right)_\tau = \left(-\frac{\mathrm{d}\dot{y}^\diamond}{\mathrm{d}\Theta}\tau\cos\Theta, R + \frac{\mathrm{d}\dot{x}^\diamond}{\mathrm{d}\Theta}\tau\cos\Theta - \frac{\mathrm{d}\dot{z}^\diamond}{\mathrm{d}\Theta}\tau\sin\Theta, \frac{\mathrm{d}\dot{y}^\diamond}{\mathrm{d}\Theta}\tau\sin\Theta\right)\mathrm{d}R\,\mathrm{d}\Theta. \tag{2.30}$$

where $\boldsymbol{x} = (x, y, z)$. Here, the derivatives of the zenithal angle can be computed from

$$\frac{\mathrm{d}\dot{x}_i^\diamond}{\mathrm{d}\Theta} = \frac{\partial \dot{x}_i^\diamond}{\partial \bar{k}_x^\diamond}\frac{\mathrm{d}\bar{k}_x^\diamond}{\mathrm{d}\Theta} + \frac{\partial \dot{x}_i^\diamond}{\partial \bar{k}_z^\diamond}\frac{\mathrm{d}\bar{k}_z^\diamond}{\mathrm{d}\Theta} \quad (i = 1, 2 \text{ or } 3), \tag{2.31}$$

where

$$\frac{\mathrm{d}\bar{k}_x^\diamond}{\mathrm{d}\Theta} = \frac{\cos\Theta}{(1 - M_1^2\cos^2\Theta)^{3/2}}, \tag{2.32}$$

$$\frac{\mathrm{d}\bar{k}_z^\diamond}{\mathrm{d}\Theta} = -\frac{\sin\Theta}{(1 - M_1^2\cos^2\Theta)^{3/2}}. \tag{2.33}$$

Furthermore, the ray direction is defined by (2.27)–(2.29) namely $\dot{\boldsymbol{x}}^\diamond = (\dot{x}^\diamond, \dot{y}^\diamond, \dot{z}^\diamond)$, which is independent of τ. With the Jacobian (2.30), the area ratio of the cross-section of the ray tube can be expressed as follows:

$$\frac{J(R,\Theta,\tau)}{J(R,\Theta,0)} = \frac{\left|\left(\dfrac{\partial \boldsymbol{x}}{\partial R}\times\dfrac{\partial \boldsymbol{x}}{\partial \Theta}\right)_\tau \cdot \dot{\boldsymbol{x}}^\diamond\right|}{\left|\left(\dfrac{\partial \boldsymbol{x}}{\partial R}\times\dfrac{\partial \boldsymbol{x}}{\partial \Theta}\right)_0 \cdot \dot{\boldsymbol{x}}^\diamond\right|}$$

$$= \frac{R\dot{y}^\diamond - \left(\dot{x}^\diamond\dfrac{\mathrm{d}\dot{y}^\diamond}{\mathrm{d}\Theta} - \dot{y}^\diamond\dfrac{\mathrm{d}\dot{x}^\diamond}{\mathrm{d}\Theta}\right)\tau\cos\Theta - \left(\dot{y}^\diamond\dfrac{\mathrm{d}\dot{z}^\diamond}{\mathrm{d}\Theta} - \dot{z}^\diamond\dfrac{\mathrm{d}\dot{y}^\diamond}{\mathrm{d}\Theta}\right)\tau\sin\Theta}{R\dot{y}^\diamond}. \tag{2.34}$$

Along the ray tube, the Blokhintzev invariant (Blokhintzev 1946),

$$\frac{\hat{p}^2 S|\boldsymbol{u} + a\nabla\varphi/|\nabla\varphi\|}{(1 - \lambda\boldsymbol{u}\cdot\nabla\varphi)},$$

must be conserved. Here, $\hat{p}$ is the acoustic pressure amplitude, S is the cross-section area normal to the ray direction, and φ is the phase ($\omega r\varphi$ is the non-dimensional phase). Since the mean velocity profile is uniform in $y > +\epsilon$, only the cross-section area S changes along the ray tube. As seen in the two-dimensional case, after the derivative matching is applied to (2.13), the final result can be formulated as

$$\hat{G}_{(3)}^{RF,low}(r,\theta,\phi \mid \omega,0,\eta,0) \approx \frac{\sqrt{J(R,\Theta,0)}}{2\pi\omega R^2\sqrt{J(R,\Theta,\tau)}}\frac{(\bar{n}_2^\diamond)^4}{(\bar{n}_1^\diamond)^2(\bar{n}_\eta^\diamond)^2(1 - M_1^2\cos^2\Theta)}$$
$$\times\frac{\exp\left[\mathrm{i}\omega r\left(\bar{k}_x^\diamond\sin\theta\cos\phi + \sqrt{(\bar{n}_2^\diamond)^2 - (\bar{k}_x^\diamond)^2 - (\bar{k}_z^\diamond)^2}\sin\theta\sin\phi + \bar{k}_z^\diamond\cos\theta\right) + \mathrm{i}\pi/2\right]}{(\bar{n}_2^\diamond)^2 - (\bar{k}_x^\diamond)^2 - (\bar{k}_z^\diamond)^2}. \tag{2.35}$$

The decay rate of refracted arrival waves in the far field falls off as $r^{-1/2}$ in the ray direction as opposed to r^{-1} in the geometrical acoustic contribution. Thus, refracted arrival waves become appreciable in the zone of silence.

2.4. *High-frequency Green's function for refracted arrival waves*

As the frequency increases, the amplitude of refracted arrival waves becomes much greater than that predicted in the low-frequency limit. To estimate such high-frequency refracted arrival waves, one must carefully analyse their behaviour near the turning point. For velocity and temperature profiles that approach the free-stream exponentially, the amplitude of refracted arrival waves in the far field was

explicitly formulated based on geometrical acoustics by Suzuki & Lele (2002). Even if the velocity and temperature profiles do not exactly satisfy such a condition, one can expect that estimates based on curve-fitting near the turning point should provide reasonable results. This section only shows the resultant formulas for refracted arrival waves in accordance with the current notation in the high-frequency limit.

Assume the temperature to be constant and the free-stream Mach numbers to be $M_1 > M_2$, and consider refracted arrival waves on the upper side downstream. Moreover, below the mixing layer, assume that the velocity profile approaches that of the free stream as $M(y) \to M_1 - \Delta M\, \mathrm{e}^{\alpha y}$ as $y \to -\infty$ (where ΔM and α are arbitrary constants determined by the velocity profile). Consequently, the amplitude can be formulated as

$$\hat{G}^{RF,high}_{(2)}(r, \phi \mid \omega, 0, \eta) \approx \frac{\sqrt{2\pi}}{2\omega^{1/2}\alpha r^{3/2}(\cos\phi - \sin\phi/\tan\phi^{\diamond})^{3/2}} \frac{\bar{n}_2^{\diamond}}{(\bar{n}_\eta^{\diamond})^{3/2}\sqrt{|\sin\phi_\eta|}} \times \frac{\exp[\mathrm{i}\omega r \varphi(\bar{k}_x^{\diamond})]}{((\bar{n}_2^{\diamond})^2 - (\bar{k}_x^{\diamond})^2)^{1/4}(1 + M_\eta^2 + 2M_\eta \bar{k}_x^{\diamond}/\bar{n}_\eta^{\diamond})^{1/4}}, \tag{2.36}$$

where $\bar{k}_x^{\diamond}$ is given by (2.20) and ϕ_η is defined by

$$\phi_\eta \equiv \arctan\left[\frac{(\mathrm{d}y/\mathrm{d}t)_\eta}{(\mathrm{d}x/\mathrm{d}t)_\eta}\right] = \arctan\left[-\frac{\sqrt{(\bar{n}_\eta^{\diamond})^2 - (\bar{k}_x^{\diamond})^2}}{(1 - M_\eta^2)\bar{k}_x^{\diamond} + M_\eta}\right]. \tag{2.37}$$

In the free stream the phase part becomes a function of $\varphi \sim \bar{k}_x^{\diamond}\cos\phi + \sqrt{(\bar{n}_2^{\diamond})^2 - (\bar{k}_x{}^{\diamond})^2}\sin\phi$. Expression (2.36) is only valid when the source is located above or close to the centreline of the mixing layer (roughly $\eta > -0.5\delta_V/\lambda$ where δ_V denotes the vorticity thickness defined later). By comparing (2.36) with (2.24), the decay rates are seen to be the same in both cases ($r^{-3/2}$), and the forms of the solution are both general plane waves. However, the proportionality of the frequency is different: $\omega^{-3/2}$ in the low-frequency limit and $\omega^{-1/2}$ in the high-frequency limit. Thus, at high-frequencies the amplitude tends to be higher than the prediction based on the vortex sheet model. Note that as the effective thickness of the mixing layer increases (as α decreases), the amplitude increases. As Suzuki & Lele (2002) reported, even when the source is located below the mixing layer, the vortex sheet model under-estimates the amplitude when the frequency is sufficiently high. The formula of refracted arrival waves on the bottom side can be similarly formulated by redefining α and replacing the subscript 2 by 1.

To derive the three-dimensional formula at high-frequencies, the ray tube theory is applied as shown in § 2.3; however, unlike the low-frequency limit the phase matching relations between the upper and lower sides are not apparent. Instead, we use the fact that an inverse Fourier transform of (2.24) yields (2.35) using the stationary phase method in the spanwise direction. As seen in (2.16), if $\tau \gg \epsilon$, the stationary point in the high-frequency limit can be approximated by that in the low-frequency limit. Therefore, the inverse Fourier transform in the high-frequency limit becomes analogous to that in the low-frequency limit. Based on (2.36) retaining $\bar{k}_z$, the three-

dimensional formula can be obtained as follows:

$$\hat{G}^{RF,high}_{(3)}(r,\theta,\phi \mid \omega,0,\eta,0) \approx \frac{\mathrm{e}^{\mathrm{i}\omega\tau}\sqrt{J(R,\Theta,0)}}{2\pi\sqrt{J(R,\Theta,\tau)}} \int_{-\infty}^{\infty} \frac{\sqrt{2\pi}\bar{n}_2^\diamond \sqrt[4]{1-(\bar{k}_z^\diamond)^2(1-M_1^2)}}{2\omega^{1/2}\alpha(\bar{n}_\eta^\diamond)^{3/2}\sqrt{\sin\theta_\eta|\sin\phi_\eta|}}$$

$$\times \frac{\exp[\mathrm{i}\omega R(\bar{k}_x^\diamond \sin\Theta + \bar{k}_z^\diamond \cos\Theta) - \mathrm{i}\omega r\Delta\varphi]}{R^{3/2}\sin^{3/2}\Theta((\bar{n}_2^\diamond)^2-(\bar{k}_x^\diamond)^2-(\bar{k}_z^\diamond)^2)^{1/4}(1+M_\eta^2+2(M_\eta\bar{k}_x^\diamond/\bar{n}_\eta^\diamond)-(\bar{k}_z^\diamond)^2/(\bar{n}_\eta^\diamond)^2)^{1/4}}\,\mathrm{d}k_z$$

$$\approx \frac{\sqrt{J(R,\Theta,0)}}{2\alpha R^2\sqrt{J(R,\Theta,\tau)}} \frac{\bar{n}_2^\diamond}{(\bar{n}_\eta^\diamond)^{3/2}\sqrt{\sin\Theta|\sin\phi_\eta|}(1-M_1^2\cos^2\Theta)}$$

$$\times \frac{\exp[\mathrm{i}\omega r\varphi(\bar{k}_x^\diamond,\bar{k}_z^\diamond)]}{((\bar{n}_2^\diamond)^2-(\bar{k}_x^\diamond)^2-(\bar{k}_z^\diamond)^2)^{1/4}(1+M_\eta^2+2(M_\eta\bar{k}_x^\diamond/\bar{n}_\eta^\diamond)-(\bar{k}_z^\diamond)^2/(\bar{n}_\eta^\diamond)^2)}, \tag{2.38}$$

where the definitions of $J(R,\Theta,\tau)$, $\bar{k}_x$, $\bar{k}_z$, etc. are the same as for (2.35), $\Delta\varphi$ denotes an arbitrary phase shift, and ϕ_η is defined by

$$\phi_\eta \equiv \arctan\left[\frac{(\mathrm{d}y/\mathrm{d}t)_\eta}{(\mathrm{d}x/\mathrm{d}t)_\eta}\right] = \arctan\left[-\frac{\sqrt{(\bar{n}_\eta^\diamond)^2-(\bar{k}_x^\diamond)^2-(\bar{k}_z^\diamond)^2}}{(1-M_\eta^2)\bar{k}_x^\diamond + M_\eta}\right]. \tag{2.39}$$

Here, the stationary phase method is applied just above the mixing layer, and the rest of the path is extended by the ray tube theory. In the free stream the phase part becomes a function of $\varphi \sim \bar{k}_x^\diamond \sin\theta\cos\phi + \sqrt{(\bar{n}_2^\diamond)^2-(\bar{k}_x^\diamond)^2-(\bar{k}_z^\diamond)^2}\sin\theta\sin\phi + \bar{k}_z^\diamond\cos\theta$. Again, the forms of the solution in the low- and high-frequency limits are similar, but the proportionality is different: ω^{-1} in the low-frequency limit and no frequency dependence in the high-frequency limit.

2.5. *Instability waves*

When the excitation frequency is sufficiently low, the forced response in the mixing layer includes instability waves. Waves of this type correspond to a discrete eigenmode whose wavenumber becomes complex and causes exponential growth. This section describes a method, called the normal mode decomposition (Ahluwalia & Keller 1977), which predicts the amplitude of instability waves excited by a time-harmonic source in the linear regime.

The basic procedure is described in § 2.3 of Part 2 (Suzuki & Lele 2003) to analyse channelled waves in a boundary layer: the method developed by Salwen & Grosch (1981) for the Orr–Sommerfeld equation is modified for inviscid compressible flows. Since the discussion in Part 2 is presented in general terms, only the essential elements are outlined here.

Consider an inviscid isothermal transversely sheared flow in two dimensions. One can express the acoustic field as a superposition of the discrete and continuous modes of the governing wave equation: in the present case the transformed third-order convective wave operator. Here, the discrete modes are exponentially decaying in the vertical direction and called the 'normal modes' in this paper. By contrast, the continuous modes have oscillatory behaviour as $y \to \pm\infty$, which are responsible for the radiated sound waves. The mode shapes in the vertical direction are given by $A(y)$ for the discrete modes and $B(k_x, y)$ for the continuous modes. Using these two types

of modes, the pressure field can be expressed as follows:

$$\Pi_{(2)}(t,x,y) = \begin{cases} \mathrm{e}^{-\mathrm{i}\omega t}\left[\displaystyle\sum_{m_-=1}^{N_-} \alpha_{m_-} A_{m_-}(y)\,\mathrm{e}^{\mathrm{i}k_{xm_-}x} + \int_{-\infty}^{0} B_-(k_x,y)\,\mathrm{e}^{\mathrm{i}k_x x}\,\mathrm{d}k_x\right] & \text{if } x<0, \\ \mathrm{e}^{-\mathrm{i}\omega t}\left[\displaystyle\sum_{m_+=1}^{N_+} \alpha_{m_+} A_{m_+}(y)\,\mathrm{e}^{\mathrm{i}k_{xm_+}x} + \int_{0}^{+\infty} B_+(k_x,y)\,\mathrm{e}^{\mathrm{i}k_x x}\,\mathrm{d}k_x\right] & \text{if } x>0, \end{cases} \tag{2.40}$$

where $\mathrm{Re}[k_{xm_-}] < 0$ and $\mathrm{Re}[k_{xm_+}] > 0$. The wavenumber is given by k_x instead of $\omega\bar{k}_x$ for later convenience, and α_m is the complex coefficient of the mth normal mode. Among these eigenfunctions, the one whose imaginary part of the wavenumber causes exponential growth needs to be extracted. When a mixing layer velocity profile has a single inflection point, only one such mode can be found downstream; namely, $\mathrm{Re}[k_{xm_+}] > 0$ and $\mathrm{Im}\,[k_{xm_+}] < 0$ in $x > 0$. Now, the normal modes (all $A_{m_\pm}(y)$) must satisfy the transformed third-order convective wave operator,

$$\mathscr{L}A_m(y) \equiv (\omega - k_{xm}M)\frac{\mathrm{d}^2A_m}{\mathrm{d}y^2} + 2k_{xm}\frac{\mathrm{d}M}{\mathrm{d}y}\frac{\mathrm{d}A_m}{\mathrm{d}y} + (\omega - k_{xm}M)[(\omega - k_{xm}M)^2 - k_{xm}^2]A_m = 0, \tag{2.41}$$

with the boundary conditions given by

$$A_m \to 0 \quad \text{as} \quad y \to \pm\infty. \tag{2.42}$$

To normalize the eigenfunctions, the adjoint operator of the convective wave equation is defined as follows:

$$\mathscr{L}^\dagger A_n^\dagger(y) \equiv (\omega - k_{xn}M)\frac{\mathrm{d}^2A_n^\dagger}{\mathrm{d}y^2} - 4k_{xn}\frac{\mathrm{d}M}{\mathrm{d}y}\frac{\mathrm{d}A_n^\dagger}{\mathrm{d}y} + (\omega - k_{xn}M)\left[(\omega - k_{xn}M)^2 - k_{xn}^2 - \frac{3k_{xn}(\mathrm{d}^2M/\mathrm{d}y^2)}{\omega - k_{xn}M}\right]A_n^\dagger = 0, \tag{2.43}$$

with the boundary conditions given by

$$A_n^\dagger \to 0 \quad \text{as} \quad y \to \pm\infty. \tag{2.44}$$

Likewise, $B(k_x,y)$ and $B^\dagger(k_x,y)$ satisfy the convective wave operator and its adjoint operator (2.41) and (2.43), respectively, but their boundary conditions are replaced by

$$\frac{\mathrm{d}B}{\mathrm{d}y} \to \mp\mathrm{i}\sqrt{(\omega - k_xM_J)^2 - k_x^2}\,B \quad \text{as} \quad y \to \mp\infty \quad (J = 1 \text{ or } 2), \tag{2.45}$$

$$\frac{\mathrm{d}B^\dagger}{\mathrm{d}y} \to \mp\mathrm{i}\sqrt{(\omega - k_xM_J)^2 - k_x^2}\,B^\dagger \quad \text{as} \quad y \to \mp\infty \quad (J = 1 \text{ or } 2). \tag{2.46}$$

Using (2.41) and (2.43), the following conservation form can be derived:

$$\int_{-\infty}^{+\infty} \Pi_n^\dagger[\mathscr{L}(\omega_m,k_{xm})\Pi_m]\,\mathrm{d}y + \int_{-\infty}^{+\infty} \Pi_m[\mathscr{L}^\dagger(\omega_n,k_{xn})\Pi_n^\dagger]\,\mathrm{d}y = \frac{\partial}{\partial t}\int_{-\infty}^{+\infty} J_t(\Pi_n^\dagger,\Pi_m)\,\mathrm{d}y + \frac{\partial}{\partial x}\int_{-\infty}^{+\infty} J_x(\Pi_n^\dagger,\Pi_m)\,\mathrm{d}y, \tag{2.47}$$

where

$$\Pi_m = A_m(y)\,\mathrm{e}^{-\mathrm{i}(\omega_m t - k_{xm}x)}, \quad \Pi_n^\dagger = A_n^\dagger(y)\,\mathrm{e}^{\mathrm{i}(\omega_n t - k_{xn}x)}, \tag{2.48}$$

$$J_t(\Pi_n^\dagger, \Pi_m) = \Pi_n^\dagger \frac{\partial^2 \Pi_m}{\partial t^2} + \Pi_m \frac{\partial^2 \Pi_n^\dagger}{\partial t^2} - \frac{\partial \Pi_n^\dagger}{\partial t}\frac{\partial \Pi_m}{\partial t} + 3M\left(\Pi_n^\dagger \frac{\partial^2 \Pi_m}{\partial t\,\partial x} + \Pi_m \frac{\partial^2 \Pi_n^\dagger}{\partial t\,\partial x}\right) + (1-3M^2)\frac{\partial \Pi_n^\dagger}{\partial x}\frac{\partial \Pi_m}{\partial x} - \Pi_n^\dagger \frac{\partial^2 \Pi_m}{\partial y^2}, \tag{2.49}$$

and

$$J_x(\Pi_n^\dagger, \Pi_m) = -3M\frac{\partial \Pi_n^\dagger}{\partial t}\frac{\partial \Pi_m}{\partial t} - (1-3M^2)\left(\Pi_n^\dagger \frac{\partial^2 \Pi_m}{\partial t\,\partial x} + \Pi_m \frac{\partial^2 \Pi_n^\dagger}{\partial t\,\partial x}\right) - (M - M^3)\left(\Pi_n^\dagger \frac{\partial^2 \Pi_m}{\partial x^2} + \Pi_m \frac{\partial^2 \Pi_n^\dagger}{\partial x^2} - \frac{\partial \Pi_n^\dagger}{\partial x}\frac{\partial \Pi_m}{\partial x}\right) - M\Pi_n^\dagger \frac{\partial^2 \Pi_m}{\partial y^2} + 2\frac{\mathrm{d}M}{\mathrm{d}y}\Pi_n^\dagger \frac{\partial \Pi_m}{\partial y}. \tag{2.50}$$

Since the eigenfunctions of the discrete modes decay exponentially as $y \to \pm\infty$, the boundary terms are not explicitly written in (2.47). Note that every product, even between a discrete mode and a continuous mode, vanishes as $y \to \pm\infty$, but this system is invalid between two continuous modes because the boundary terms remain.

As discussed in Part 2, $\int_{-\infty}^{+\infty} J_x \,\mathrm{d}y$ behaves as an 'inner product' in a spatial problem, by which a bi-orthogonal system is established for discrete modes. $\int_{-\infty}^{+\infty} J_t \,\mathrm{d}y$ shown above also behaves as an inner product in a temporal problem. Following the procedure described in Part 2, we calculate the following inner product to determine the coefficient a_n:

$$J_x\left(\Pi_n^\dagger, \mathrm{e}^{-\mathrm{i}\omega t}\left[\sum_{m_+=1}^{N_+} a_{m_+} A_{m_+}\,\mathrm{e}^{\mathrm{i}k_{xm_+}x} + \int_0^{+\infty} B_+(k_x, y)\,\mathrm{e}^{\mathrm{i}k_x x}\,\mathrm{d}k_x - \sum_{m_-=1}^{N_-} a_{m_-} A_{m_-}\mathrm{e}^{\mathrm{i}k_{xm_-}x} - \int_{-\infty}^{0} B_-(k_x, y)\,\mathrm{e}^{\mathrm{i}k_x x}\mathrm{d}k_x\right]\right) = J_x(\Pi_n^\dagger, a_n \Pi_n). \tag{2.51}$$

After some calculation, this yields

$$\alpha_n^{IN} = \frac{-\mathrm{i}\,(\omega - k_{xn}M_\eta)A_n^\dagger(\eta)}{\displaystyle\int_{-\infty}^{+\infty} \hat{J}_x(\omega, k_{xn}, k_{xn}, A_n^\dagger, A_n)\,\mathrm{d}y}, \tag{2.52}$$

where

$$\hat{J}_x(\omega, k_{xn}, k_{xm}, A_n^\dagger, A_m) = \left[-3\omega^2 M - \omega(k_{xn}+k_{xm})(1-3M^2) + (k_{xn}^2 + k_{xn}k_{xm} + k_{xm}^2)(M - M^3)\right] A_n^\dagger A_m - MA_n^\dagger \frac{\mathrm{d}^2 A_m}{\mathrm{d}y^2} + 2\frac{\mathrm{d}M}{\mathrm{d}y}A_n^\dagger \frac{\mathrm{d}A_m}{\mathrm{d}y}. \tag{2.53}$$

Here, the superscript 'IN' stands for instability waves. It should be emphasized that α_n^{IN} is proportional to the value of the adjoint eigen-shape at the source position; thus, the shape of the adjoint eigenmode indicates the receptivity to the source position. $A_m(y)$ and $A_n^\dagger(y)$ are computed based on the initial mixing layer velocity profile of DNS. This theoretical prediction is compared with the DNS data in § 4.3. Finally, the

Case	Figure numbers	$Re \equiv U_\infty \delta_V / \nu$	λ/δ_V	A_0	σ_p	η	Ro
Case A	4, 8–11	5×10^3	4.0	$5. \times 10^{-3}$	0.0075	0.	12
Case B	5, 12–15	5×10^4	1.0	$5. \times 10^{-3}$	0.025	0.	14
Case C	6, 16–19	5×10^5	0.25	$5. \times 10^{-3}$	0.040	0.	20
Case D	20–28	1×10^5	16.0	$1. \times 10^{-5}$	0.001875	0.	—
Case E	23, 24	1×10^5	16.0	$1. \times 10^{-5}$	0.001875	−0.0125	—
Case F	25, 26	2.5×10^3	16.0	$1. \times 10^{-5}$	0.001875	0.	—

Case	Δt	(N_x, N_y)	$(\Delta x_{max}, \Delta y_{max})$	$(\Delta x_{min}, \Delta y_{min})$
Case A	1/640	(1200, 720)	(0.0375, 0.0600)	(0.00375, 0.00376)
Case B	1/320	(840, 800)	(0.05, 0.05)	(0.00625, 0.00632)
Case C	1/160	(1120, 1080)	(0.048, 0.048)	(0.016, 0.016)
Case D	1/2560	(1000, 360)	(0.00938, 0.03118)	(0.000938, 0.000948)
Case E	1/2560	(1000, 360)	(0.00938, 0.03118)	(0.000938, 0.000948)
Case F	1/2560	(1000, 360)	(0.00938, 0.03118)	(0.000938, 0.000948)

TABLE 1. Parameters for the DNS.

three-dimensional formula can be expressed as follows:

$$\Pi_{(3)}(t,x,y,z) = \frac{e^{-i\omega t}}{2\pi} \sum_{m=1}^{N} \left[\int_{-\infty}^{+\infty} a_m(k_z) A_m(y,k_z) e^{i[k_{xm}(k_z)x + k_z z]}\, dk_z + \int_0^{+\infty} \int_{-\infty}^{+\infty} B(k_x,y,k_z) e^{i(k_x x + k_z z)}\, dk_z\, dk_x \right], \quad (x \geqslant 0_+), \tag{2.54}$$

and the coefficient $a_m^{IN}(k_z)$ can be similarly determined.

3. Numerical procedures

To compare the theoretical predictions with the numerical simulation, the full Navier–Stokes equations were explicitly solved using direct numerical simulation (DNS). For time marching, the standard fourth-order Runge–Kutta scheme was used. For spatial differencing, the sixth-order Padé scheme (Lele 1992) was used for the interior points. For the boundary points, lower-order (third and fourth) Padé schemes were used (Lele 1992). The grid size, time step, etc. are shown in table 1.

To prevent spurious reflection of acoustic waves from the computational boundaries, a so-called 'damping-sponge' (Freund 1997) was used together with the non-reflecting boundary conditions (Giles 1990). For the detailed procedures and the code validation, refer to Suzuki (2001).

For the initial velocity field, the compressible boundary layer equation was solved using the Illingworth–Stewartson transformation with the boundary conditions of $M_1 = 0.8$, $\rho_1 = 1$ and $T_1 = 1$ at $y = -\infty$, and $M_2 = 0$, $\rho_2 = 1$ and $T_2 = 1$ at $y = \infty$. Based on this velocity profile, the initial temperature and density were computed using the Crocco–Busemann relation. The Prandtl number was set to $Pr = 0.7$. The rest of the conditions (the Reynolds number and other parameters) are also shown in table 1. Recall that all quantities are normalized by the acoustic wavelength λ and the ambient speed of sound a_∞, unless otherwise noted. The vorticity thickness is defined by

$$\delta_V = \left. \frac{U_1 - U_2}{(\partial U/\partial y)_{max}} \right|_{x=0}, \tag{3.1}$$

where the velocity profile was set so that $\partial U/\partial y$ takes its maximum at $y = 0$. Note that the Reynolds numbers are defined based on the vorticity thickness (see table 1) and set as high as possible, so that the viscous effect and the spreading rate of the mixing layer were minimized (less than 1% increase of the local vorticity thickness over a distance of the acoustic wavelength for all cases).

Based on the initial velocity profile, ray trajectories were computed using the eikonal equation for reference. Here, the temperature variation was ignored for simplicity. By the method of characteristics, the ODE system was integrated using the fourth-order Runge–Kutta scheme. Refer to Suzuki (2001) for the detailed procedures. A total of 60 rays was issued in each case (every 6°), and the minimum time step was set to $\Delta t = 1/300$ which was exponentially stretched (2% increase for each time step).

To simulate a point source, the right-hand side of the Navier–Stokes equations was forced. Instead of imposing a delta function as shown in (2.6), a Gaussian-shaped source term whose narrow width limit becomes a delta function was imposed. With fine grid spacing near the source region, spurious high frequency waves can be suppressed. By following the derivation of the third-order convective wave equation, it is deduced that the following forcing terms yield such a source:

$$\frac{\partial \rho}{\partial t} + \frac{\partial(\rho u_j)}{\partial x_j} = 0, \tag{3.2}$$

$$\frac{\partial(\rho u_i)}{\partial t} + \frac{\partial(\rho u_i u_j + p\delta_{ij} + \tau_{ij})}{\partial x_j} = -A_p(t)\rho F(t, x_1, x_2)\delta_{i1}, \tag{3.3}$$

$$\frac{\partial[\rho(e + \frac{1}{2}u_k^2)]}{\partial t} + \frac{\partial[\{\rho(e + \frac{1}{2}u_k^2) + p\}u_j + \tau_{jk}u_k + q_j]}{\partial x_j} = -A_p(t)\rho u_1 F(t, x_1, x_2), \tag{3.4}$$

where

$$F(t, x_1, x_2) = \cos(-\omega t)\frac{\left[1 + \mathrm{erf}(x_1 - x_{1p}/\sqrt{2\sigma_p^2})\right]}{2}\frac{\exp[-(x_2 - x_{2p})^2/2\sigma_p^2]}{\sqrt{2\pi\sigma_p^2}} \tag{3.5}$$

and (x_{1p}, x_{2p}) denotes the centre of the source. Assuming that $|\partial u_1/\partial x_1|, |\partial u_2/\partial x_1| \ll |\partial u_1/\partial x_2|$, these source terms correspond to the following equation:

$$\frac{\mathrm{D}}{\mathrm{D}t}\left[\frac{\mathrm{D}^2\Pi}{\mathrm{D}t^2} - \frac{\partial}{\partial x_j}\left(a^2\frac{\partial \Pi}{\partial x_j}\right)\right] + 2\frac{\partial u_k}{\partial x_j}\frac{\partial}{\partial x_k}\left(a^2\frac{\partial \Pi}{\partial x_j}\right)$$

$$= \frac{\mathrm{D}}{\mathrm{D}t}\left[A_p(t)\frac{\exp\left[-\sum_{j=1}^{2}\frac{(x_j - x_{jp})^2}{2\sigma_p^2}\right]}{2\pi\sigma_p^2}\cos(-\omega t)\right]. \tag{3.6}$$

Therefore, in the limit $\sigma_P \to 0$, the right-hand side of (3.6) becomes a delta function, namely $(\mathrm{D}/\mathrm{D}t)[A_p\delta(\boldsymbol{x} - \boldsymbol{x}_p)\cos(-\omega t)]$. In the computations, the coefficient A_p was set to $A_p(t) = \frac{1}{2}A_0[1 + \mathrm{erf}((t - t_1)/\sigma_t)]$, so that the effects of spurious high-frequency waves and spurious instability waves can be lessened. Here, $\sigma_t = \pi/\omega$ and $t_1 = 2\pi/\omega$. The rest of the parameters for the forcing terms are shown in table 1.

To measure the directivity of pressure amplitude for direct waves, 120 observer points were distributed nearly every 3° on a circle centred at the source location with a radius of approximately *Ro*. They were located on the grid points of the DNS, and

Case	Observer position in y	Correction: ΔX_1, ΔX_2	α_1, α_2
Case A	$\mp 1.0\lambda$	-0.3λ, 0.9λ	72.0λ, 12.0λ
Case B	$\mp 1.0\lambda$	-0.4λ, 1.3λ	11.0λ, 3.0λ
Case C	$\mp 2.0\lambda$	-0.4λ, 4.0λ	1.75λ, 0.75λ

TABLE 2. Parameters for the comparison of refracted arrival waves. The subscripts 1 and 2 denote the lower and the upper sides, respectively. The position corrections are defined by $\Delta X \equiv r \sin\phi / \tan\phi^{\diamond}$ in (2.36).

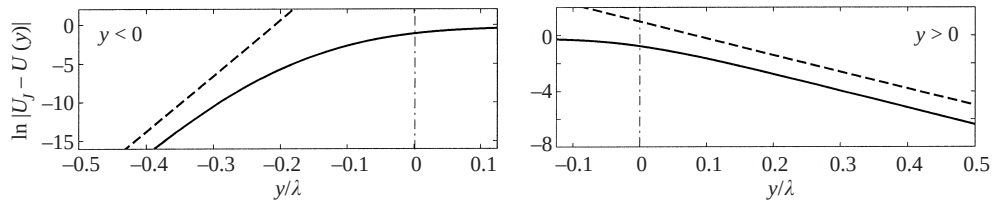

FIGURE 4. Asymptotic behaviour of the velocity profiles in Case A. The velocity deviation from the free-stream is shown in log-scale: ——, velocity profile solved using DNS; – – –, the exponential factor α adopted to calculate the high-frequency limit of refracted arrival waves.

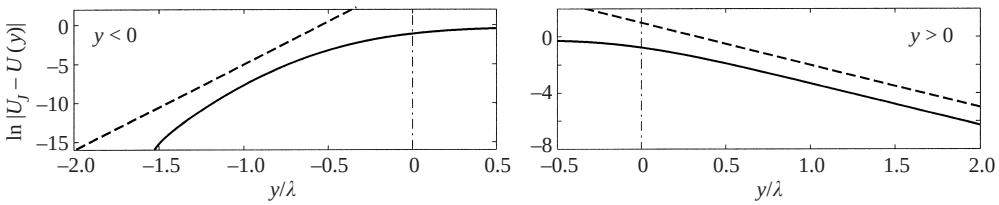

FIGURE 5. Asymptotic behaviour of the velocity profiles in Case B. Notation is the same as figure 4.

the position errors defined by $|Ro - \sqrt{(x_1 - x_{1p})^2 + (x_2 - x_{2p})^2}|$ $(\sim O(\sqrt{\Delta x^2 + \Delta y^2}))$ were corrected in the data processing. At these points, pressure profiles were recorded during two time periods of the forcing frequency. Subsequently, the pressure profile at each point was transformed into the frequency domain, and only the quantities at the forcing frequency were evaluated. To measure the amplitude profiles of refracted arrival waves, observer points were distributed upstream just below the mixing layer and downstream just above the mixing layer, and the same data-processing method was used. Correction for the curved arc-length between the centreline of the mixing layer and the observer position was evaluated based on the ray trajectories. To compare the theoretical prediction with the DNS result, the velocity profile exponent α in (2.36) was estimated from the DNS flow data using curve-fitting (see figures 4–6). The observer positions, their correction based on the ray trajectories, and the values of α are all tabulated in table 2. Since the Reynolds numbers of the numerical simulations were set to be sufficiently high, the correction for the viscous dissipation was not included. Similarly, to compare the eigenmode shapes and the magnitude of instability waves, observer points were distributed downstream of the source and the pressure data were taken during one time period of the forcing frequency.

To calculate the eigenmode shapes of instability waves, the following Riccati forms of the convective wave operator and its adjoint operator were solved using the standard fourth-order Runge–Kutta scheme based on the velocity profile obtained

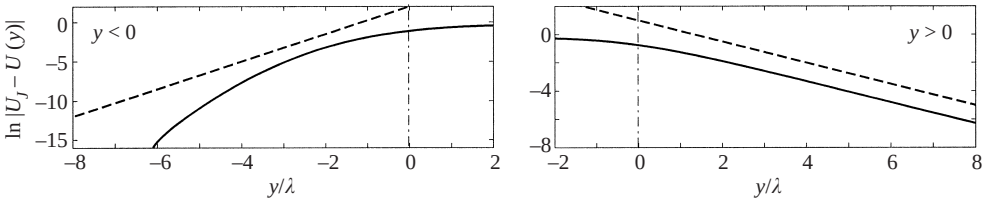

FIGURE 6. Asymptotic behaviour of the velocity profiles in Case C. Notation is the same as figure 4.

from DNS at $x = 0$:

$$\frac{\mathrm{d}Q}{\mathrm{d}y} + \left(Q + \frac{2k_x\,\mathrm{d}M/\mathrm{d}y}{\omega - k_x M}\right) Q + (n^2 - k_x^2) = 0, \tag{3.7}$$

and

$$\frac{\mathrm{d}Q^\dagger}{\mathrm{d}y} + \left(Q^\dagger - \frac{4k_x\,\mathrm{d}M/\mathrm{d}y}{\omega - k_x M}\right) Q^\dagger + \left(n^2 - k_x^2 - \frac{3k_x\,\mathrm{d}^2M/\mathrm{d}y^2}{\omega - k_x M}\right) = 0, \tag{3.8}$$

with the boundary conditions given by

$$Q(\mp\infty) = \mp\sqrt{n_J^2 - k_x^2} \quad (J = 1 \text{ or } 2), \tag{3.9}$$

and

$$Q^\dagger(\mp\infty) = \mp\sqrt{n_J^2 - k_x^2} \quad (J = 1 \text{ or } 2), \tag{3.10}$$

where $Q(y) = A'(y)/A(y)$ and $Q^\dagger(y) = A^{\dagger\prime}(y)/A^\dagger(y)$. Equations (3.7) and (3.8) were both integrated from $y = \pm y_{max}$ to the inflection point by a shooting method, and the complex wavenumbers k_{xm} were computed using the Newton–Raphson method. To compute the inner products (2.53), the trapezoidal rule (second order) was used, and the width of the source in the y-direction was taken into account in the numerical integration.

4. Results and discussion

A total of six DNS cases was computed. The first three (Cases A–C) were simulated to study the frequency dependence of sound waves, and the rest (Cases D–F) were simulated to study the receptivity of instability waves. Note that the forcing frequencies in (Cases A–C) are neutrally stable, while the frequency in Cases D–F is close to the most unstable frequency (see figure 7). Parameters of each case are tabulated in table 1.

4.1. *Overall sound radiation patterns and direct waves*

In the following, the instantaneous pressure contours, the ray trajectories, the corresponding pressure amplitudes in polar plots, and the pressure amplitude profiles of refracted arrival waves are presented. In the polar plots the results of DNS are compared with the low- and high-frequency asymptotes of both direct and refracted arrival waves. For refracted arrival waves the pressure profiles from DNS are compared with frequency asymptotes both just above and below the mixing layer.

Figures 8–11 represent the low-frequency case (Case A, see table 1). Figure 8 shows that the pressure field becomes peaked toward the critical angles defined by the high-frequency limit on both lower and upper sides. In addition, on the lower side one can see direct waves propagating beyond the critical angle as predicted in the

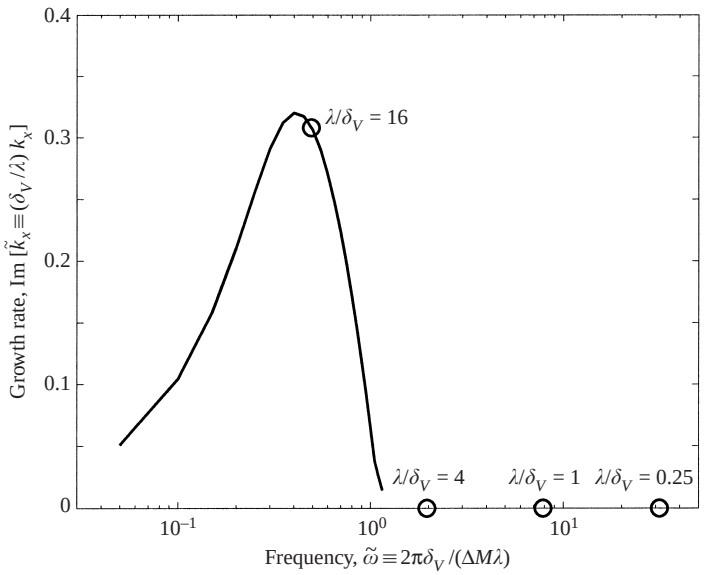

FIGURE 7. Frequency range of DNS. Dispersion relation for an inviscid mixing layer ($M_1 = 0.8$ and $M_2 = 0$) is shown. The spatial problem is solved based on the linear stability analysis.

low-frequency limit. These waves apparently have opposite phase on either side of the critical angle, and they rapidly decay upstream. In the zone of silence, refracted arrival waves appear in the form of general plane waves.

The numerical artifacts excite strong instability waves from the inflow and the source location, and they disturb direct waves and refracted arrival waves, particularly in $x > 0$. Although the polar plot (figure 10) also includes the disturbances due to these instability waves downstream, it clearly shows the correspondence between the numerical results and the asymptotic theories: figure 10 demonstrates that the directivity of direct waves solved by DNS is similar to the high-frequency limit. Although the ratio of the wavelength to the vorticity thickness is $\lambda/\delta_V = 4.0$, this is reduced by a factor of 2π when differentiating the acoustic disturbance. Thus, the actual ratio may become much smaller, and the directivity of direct waves is close to the high-frequency limit. This result confirms some previous studies (Balsa 1976; Tester & Morfey 1976) in which the high-frequency limit and experiments generally agree when the Helmholtz number is close to or less than unity. By contrast, refracted arrival waves solved using DNS agree well with the low-frequency limit. Since the effective wavenumber in the vertical direction becomes smaller near the zone of silence, one can expect that the refracted arrival waves in Case A approach the low-frequency limit more easily than the direct waves do.

Figures 12–15 represent the intermediate frequency case (Case B, see table 1). Figure 12 shows a radiation pattern fairly similar to Case A (see figure 8); however, direct waves beyond the critical angle become negligible, and the relative strength of refracted arrival waves increases. Notice that at the interfaces between the direct waves and the refracted arrival waves, there is a phase discontinuity, which can be deduced from the asymptotic theories. Figure 14 also shows good agreement between the DNS result and the high-frequency limit. Although the computational domain may not be large enough to compare with the far-field asymptotes (see figure 12), one can expect that the angles of the radiation peak in the DNS become closer to the theoretical predictions as the computational domain is extended.

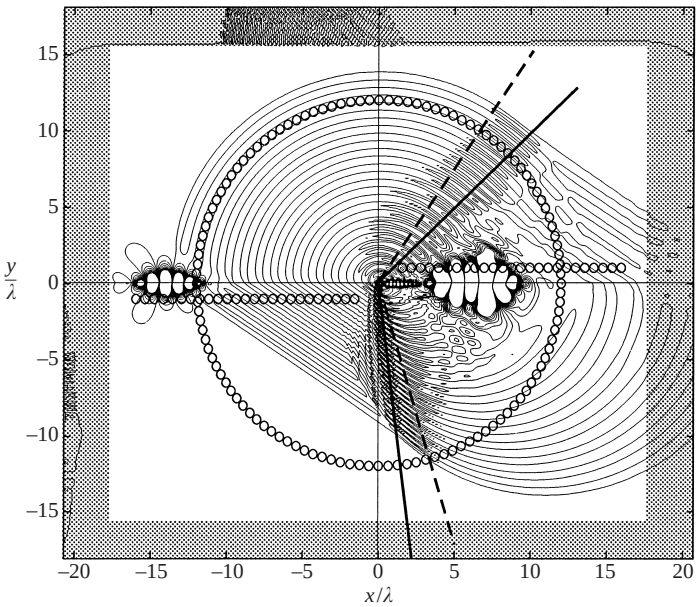

FIGURE 8. Pressure field at low-frequency, Case A ($\lambda/\delta_V = 4.0$). Instantaneous pressure contours at time $t \approx 14$ are shown. Contour level: $0.998p_\infty \sim 1.002p_\infty$ with intervals of $2.5 \times 10^{-4}p_\infty$. Peak angles based on the asymptotic theories: – – –, low-frequency limit (identical to the ray directions of refracted arrival waves); ——, high-frequency limit; ○, the points where the data were taken (at $Ro \approx 12\lambda$) to evaluate the pressure amplitude (figures 10 and 11). The shaded region depicts the sponge boundary.

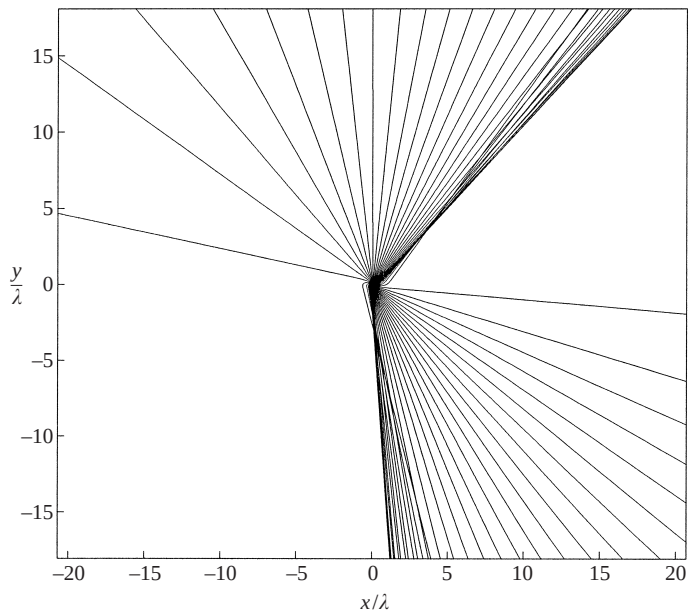

FIGURE 9. Ray trajectories at low-frequency, Case A. The eikonal equation was solved based on the initial velocity profile. The temperature variation was ignored. In total, 60 rays were solved at every 6°.

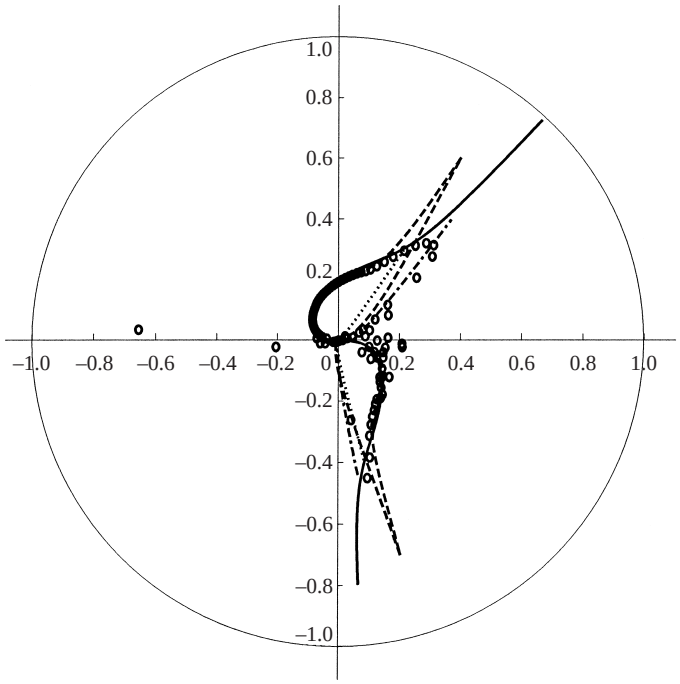

FIGURE 10. Pressure amplitude directivity at low-frequency, Case A. Pressure amplitude normalized by $\sqrt{Ro}$ (observer position $Ro \approx 12\lambda$) is shown in polar plots: – – –, low-frequency limit of direct waves; ——, high-frequency limit of direct waves; – · – · –, low-frequency limit of refracted arrival waves; · · · · · ·, high-frequency limit of refracted arrival waves; ○, DNS result corresponding to figure 8. (Pressure histories were recorded at 120 observer points after $t = 15$ on the lower side and $t = 14$ on the upper side.)

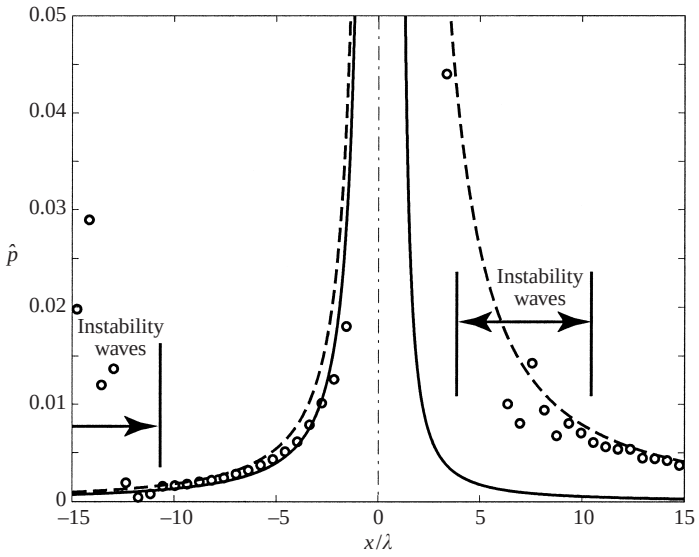

FIGURE 11. Pressure amplitude profiles of refracted arrival waves at low-frequency, Case A. Pressure amplitude profiles along the mixing layer (at $y = -1.02$ on the left-hand side and $y = +1.02$ on the right-hand side) are plotted: – – –, low-frequency limit of refracted arrival waves; ——, high frequency limit of refracted arrival waves; ○, DNS result corresponding to figure 8 was processed after $t = 12.5$ on the left-hand side and $t = 9.5$ on the right-hand side.

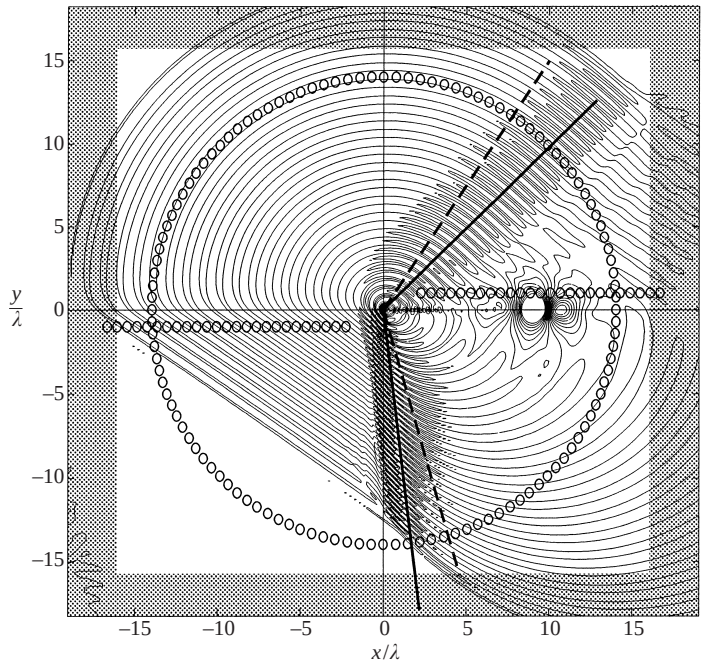

FIGURE 12. Pressure field at intermediate frequency, Case B ($\lambda/\delta_V = 1.0$). Instantaneous pressure contours at time $t \approx 20$ are shown. Contour levels and notation are the same as figure 8. The data were recorded at $Ro \approx 14\lambda$ to evaluate the pressure amplitude (figures 14 and 15).

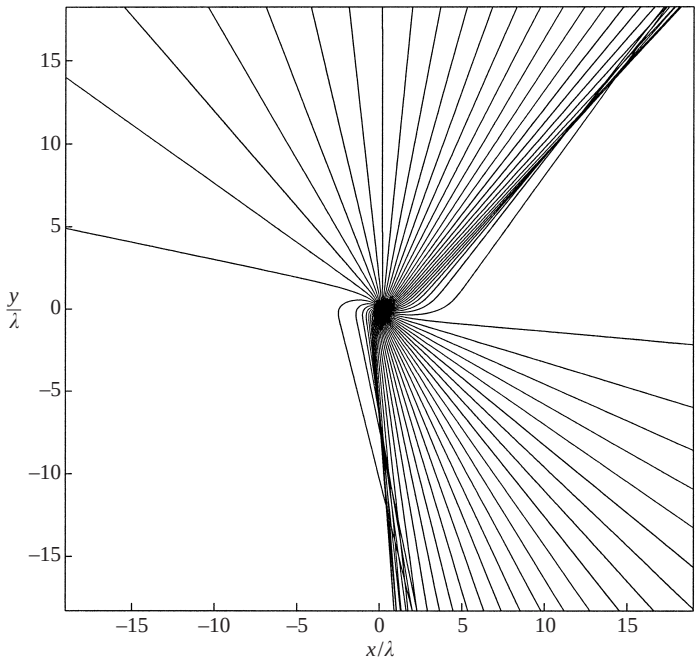

FIGURE 13. Ray trajectories at intermediate frequency, Case B.
The procedure is the same as figure 9.

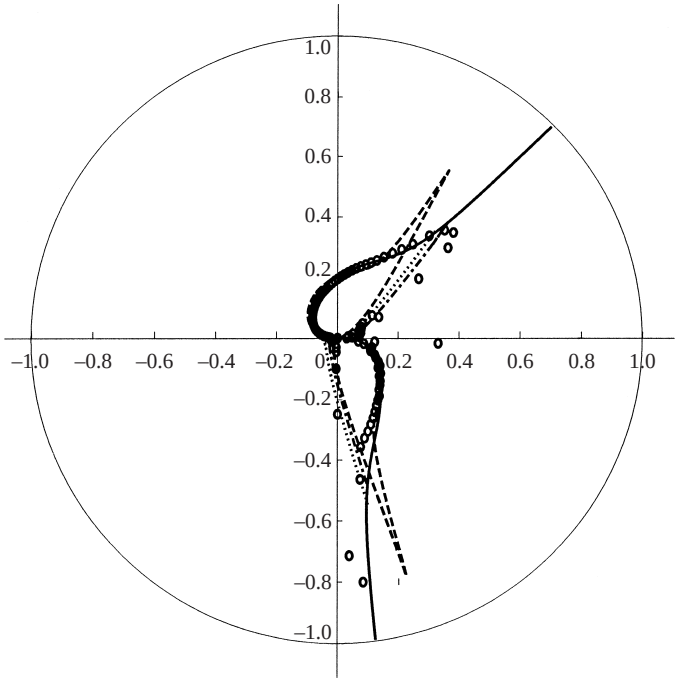

FIGURE 14. Pressure amplitude directivity at intermediate frequency, Case B. Pressure amplitude normalized by $\sqrt{Ro}$ (observer position $Ro \approx 14\lambda$) is shown in polar plots. Notation is the same as figure 10. Pressure histories were recorded after time $t = 26$ on the lower side and $t = 20$ on the upper side.

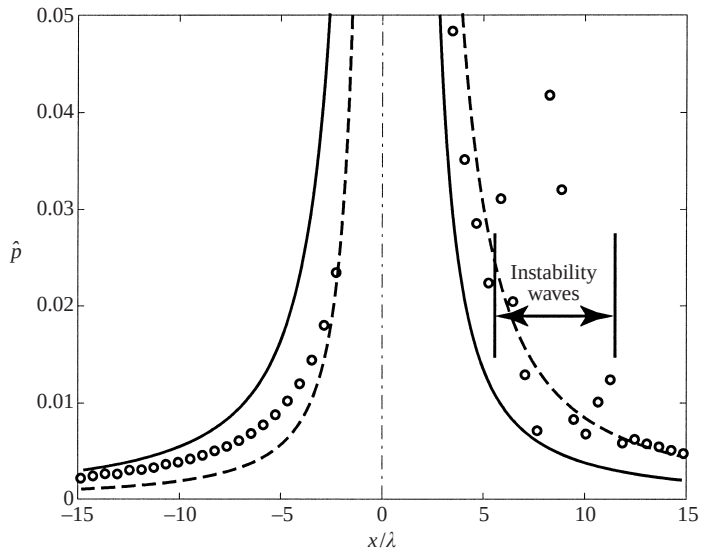

FIGURE 15. Pressure amplitude profiles of refracted arrival waves at intermediate frequency, Case B. Pressure amplitude profiles along the mixing layer (at $y = -1.01$ on the left-hand side and $y = +1.01$ on the right-hand side) are plotted: notation is the same as figure 11. DNS result corresponding to figure 12 was processed after $t = 18.5$ on the left-hand side and $t = 16.5$ on the right-hand side.

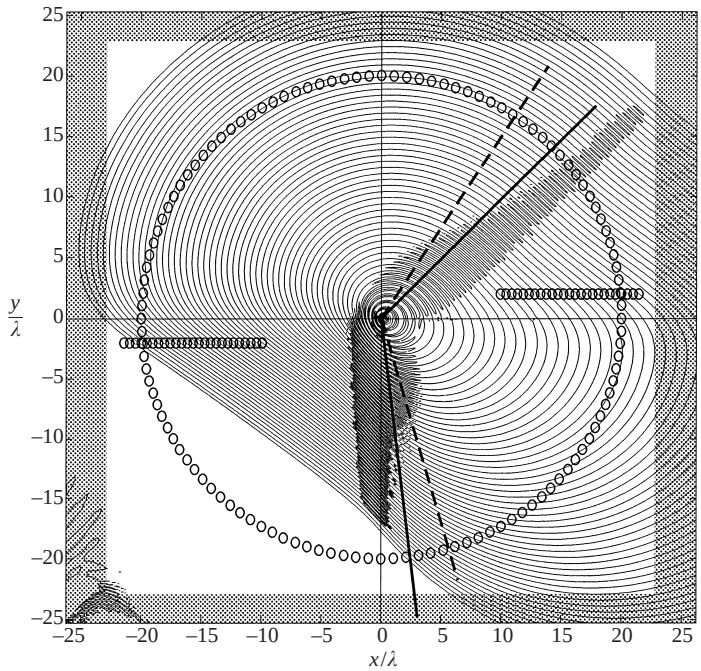

FIGURE 16. Pressure field at high-frequency, Case C ($\lambda/\delta_V = 0.25$). Instantaneous pressure contours at time $t \approx 28$ are shown. Contour levels and notation are the same as figure 8. The data were recorded at $Ro \approx 20\lambda$ to evaluate the pressure amplitude (figures 18 and 19).

Figures 16–19 represent the high-frequency case (Case C, see table 1). At high-frequencies the analysis based on geometrical acoustics is very useful. Referring to figures 16 and 17, one can readily see that the rays are focusing toward the critical angle, in which the pressure amplitude increases according to the ray tube theory. In the zone of silence, the distance between the rays becomes very large, and the angles of the rays are almost parallel to the critical angle; thus, refracted arrival waves appear in the form of general plane waves. Although their amplitude falls off faster in the flow direction ($x^{-3/2}$ in two dimensions) than that of direct waves ($x^{-1/2}$), it is preserved in the ray direction. The series of figures 8, 12 and 16 shows that the relative strength of refracted arrival waves increases as the frequency becomes higher. Figure 17 shows that the overall radiation pattern, including refracted arrival waves, approaches the high-frequency limit although the computational domain is not sufficiently large.

4.2. *Refracted arrival waves*

The series of figures 11, 15 and 19 compares the pressure amplitude of refracted arrival waves at three different frequencies. In Cases A and B the transient disturbances due to the initial source excitation cause instability waves; consequently, they disturb the amplitude profiles. Nevertheless, one can observe general trends of the frequency response from these DNS results. Case A shows very good agreement with the low-frequency limit. As the frequency increases (Case B), the pressure amplitude in the DNS on the upstream side shifts from the low- to the high-frequency limit although that on the downstream side still follows the low-frequency limit. Finally, Case C shows that the profile on the downstream side follows the high-frequency limit, and

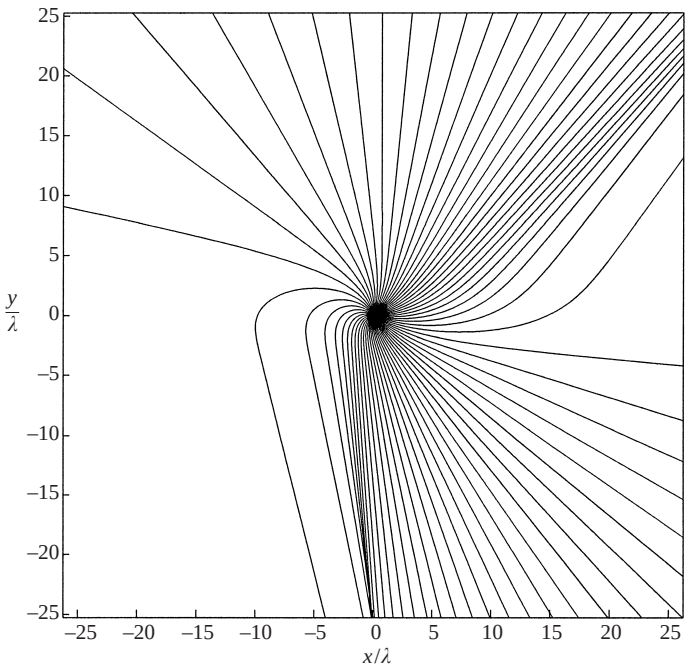

FIGURE 17. Ray trajectories at high-frequency, Case C. The procedure is the same as figure 9.

that on the upstream side also approaches the high-frequency limit. Thus, the pressure profile of refracted arrival waves tends to shift from the low- to high-frequency limit as the source frequency increases. It is important to remember that their amplitude in the high-frequency limit exceeds that in the low-frequency limit as the source frequency increases. Based on these DNS results, one can conclude that the acoustic field is predictable using geometrical acoustics when the source frequency corresponds to $\lambda/\delta_V \lesssim 1$.

In addition, these results strongly suggest that the sound pressure levels in the zone of silence should be evaluated based on refracted arrival waves instead of the extension of direct waves. Many previous studies (such as Balsa 1976; Tester & Morfey 1976; Goldstein 1982) extended the analysis for direct waves in this zone: they treated the solutions as evanescent waves inside the turning point. However, the DNS results demonstrate that the form of the solution in the zone of silence appears to be general plane waves, particularly at high frequencies.

Note that since the actual velocity profiles of the DNS do not perfectly follow the exponential form ($M(y) \sim \mathrm{e}^{\pm\alpha y}$), especially in $y < 0$ (see figures 4–6), the estimate based on the high-frequency limit downstream may not be very accurate. Moreover, the limited size of the computational domain and the steep curvature of the rays might cause some deviation from the asymptotic theories.

It should be emphasized that the analytical expressions for refracted arrival waves are strictly restricted to the parallel mean flow assumption. As discussed by Suzuki & Lele (2002), a 5% spreading rate of the mixing layer increases the pressure amplitude several times larger than a parallel mixing layer. As discussed by Khavaran & Krejsa (1994) and Tam & Auriault (1998), it might not be appropriate to assume the mean flow to be locally parallel for jets with a large spreading rate. Nonetheless, the distinction between the low- and high-frequency asymptotic expressions should

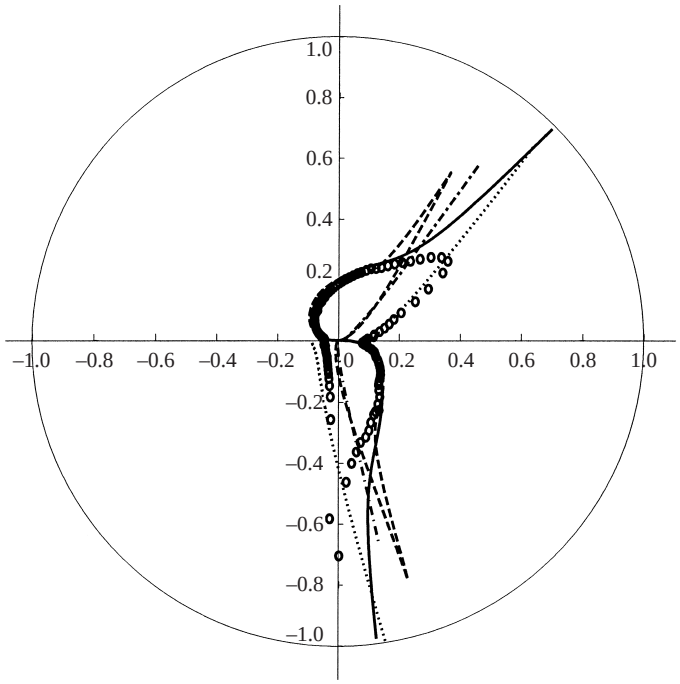

FIGURE 18. Pressure amplitude directivity at high-frequency, Case C. Pressure amplitude normalized by $\sqrt{Ro}$ (observer position $Ro \approx 20\lambda$) is shown in polar plots. Notation is the same as figure 10. Pressure histories were recorded after time $t = 41$ on the lower side and $t = 38$ on the upper side.

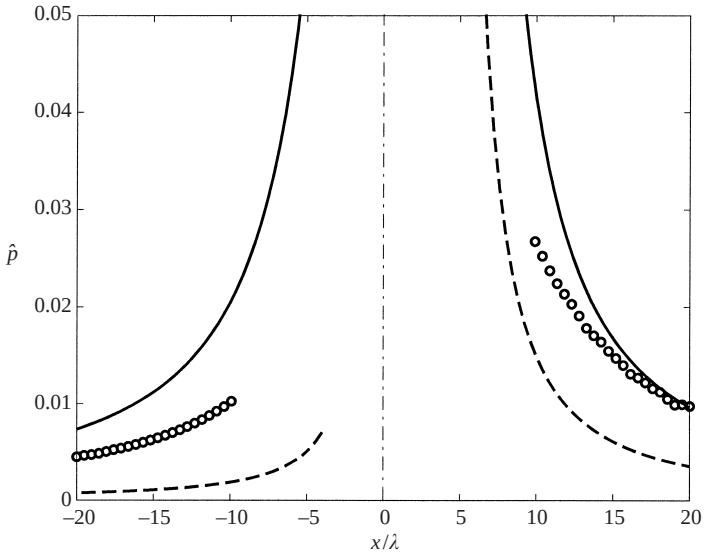

FIGURE 19. Pressure amplitude profiles of refracted arrival waves at high-frequency, Case C. Pressure amplitude profiles along the mixing layer (at $y = -2.00$ on the left-hand side and $y = +2.00$ on the right-hand side) are plotted: notation is the same as figure 11. DNS result corresponding to figure 16 was processed after $t = 28$ on both sides.

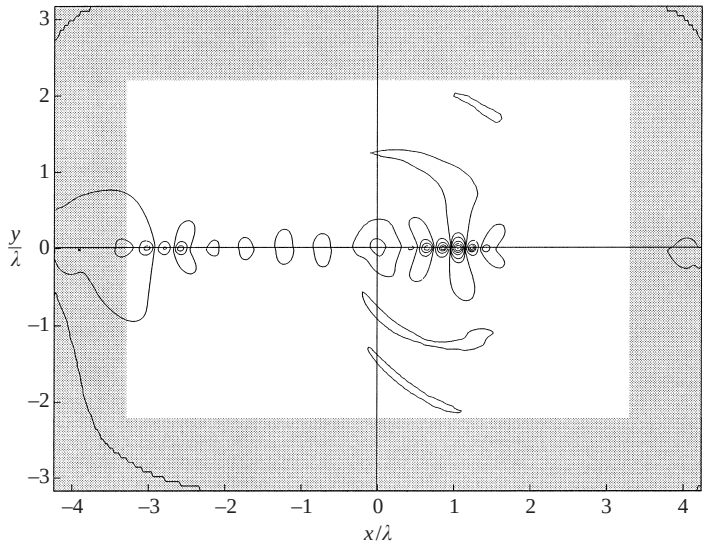

FIGURE 20. Pressure field at very low-frequency, Case D ($\lambda/\delta_V = 16.0$). Instantaneous pressure contours at time $t \approx 3$ are shown. Contour levels are the same as figure 8.

improve the prediction of sound pressure levels of refracted arrival waves from subsonic jets.

4.3. *Instability waves*

Finally, to compare the eigenmode shapes and the magnitude of instability waves, a very low-frequency source ($\lambda/\delta_V = 16.0$) was forced, a frequency slightly higher than that of the most unstable eigenmode (see figure 7). Note that in these simulations, only a single unstable mode exists at the given frequency, and this mode completely overcomes the sound waves (see figure 20).

To understand the overall picture, first observe the eigenmode shapes of the third-order convective wave operator and its adjoint operator. Figure 21 depicts the velocity profile and its derivatives in the vertical direction, and figure 22 plots both eigenmode shapes and the source size of DNS. Figure 22 shows that the eigenmode shape of the adjoint operator has a very sharp peak. One can understand this feature from the local exponents (complex wavenumbers) of the eigen-shapes by noting the sign change of the second term inside the parentheses in (3.7) and (3.8). The narrow peak suggests that the receptivity of instability waves strongly depends on the source position in the inviscid limit (see (2.52)). Moreover, the gradient of the adjoint eigenmode shape is of $O(10^1) \times \max|A^\dagger|/\delta_V$. Therefore, when the Reynolds number decreases, the viscous term becomes effective, which may be $O(10^4)/Re \times (\max|A^\dagger|/\delta_V)^4$. Remember that the viscous term of the Orr–Sommerfeld equation has a fourth-derivative term. This indicates that the viscous effect should broaden the peak of the adjoint eigenmode shape and cause the receptivity to be less sensitive to the source position. These hypotheses are verified based on the DNS results described below.

Figures 23 and 24 compare the theoretical predictions and the DNS results in terms of the pressure magnitude of instability waves for two different source positions. As described in § 2.5, multiple discrete modes may exist (see (2.40)); however, only the unstable mode becomes dominant downstream. In the near field the magnitude observed in the DNS does not agree with the theoretical prediction (see figure 23).

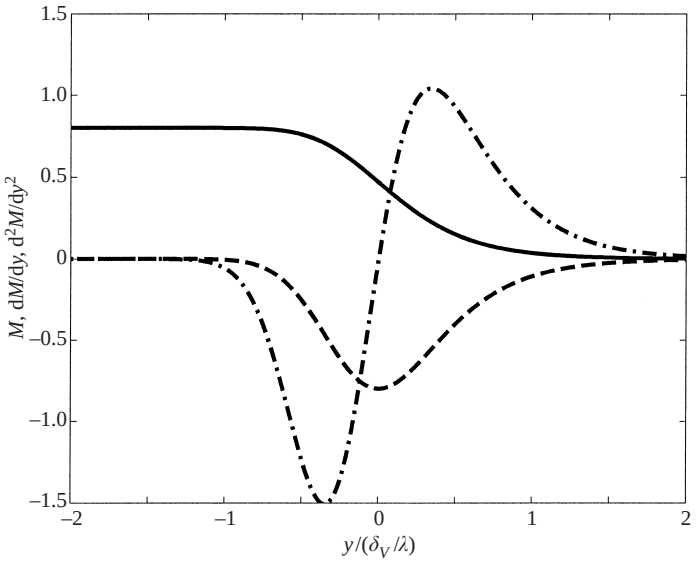

FIGURE 21. Mean velocity and its first- and second-derivative profiles. Data were taken from DNS, Case D: ——, $M(y)$; – – –, $\mathrm{d}M(y)/\mathrm{d}y$; and –·–·–, $\mathrm{d}^2M(y)/\mathrm{d}y^2$.

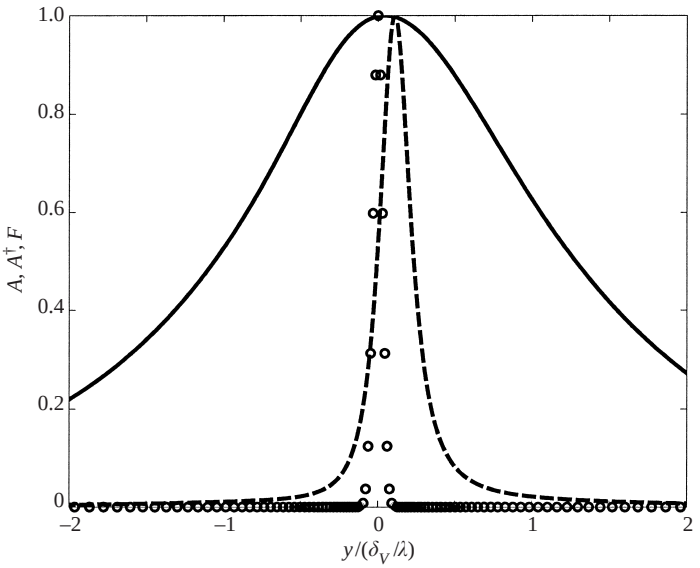

FIGURE 22. Comparison of the eigenmode shapes. The eigenmode shapes and the source size for Case D are plotted: ——, $A(y)$ (regular); – – –, $A^\dagger(y)$ (adjoint); ○, source size corresponding to the grid points of DNS (F, see equation (3.5)). All maximum values are normalized as unity.

Moreover, far downstream ($x \gtrsim 15$) instability waves have not yet reached stationary levels; thus, the magnitude deviates again downstream. But, in the middle range the agreement between the theoretical and numerical results is satisfactory. Figure 24 depicts the eigenmode shapes in the transverse direction. Although, Case D shows slightly lower magnitude ($\sim 10\%$ lower), the theory predicts the eigenmode shape and its magnitude quite well. Figure 24 also demonstrates that by slightly shifting the source position downward ($\eta = -0.2 \times \delta_V/\lambda$), the magnitude of instability waves

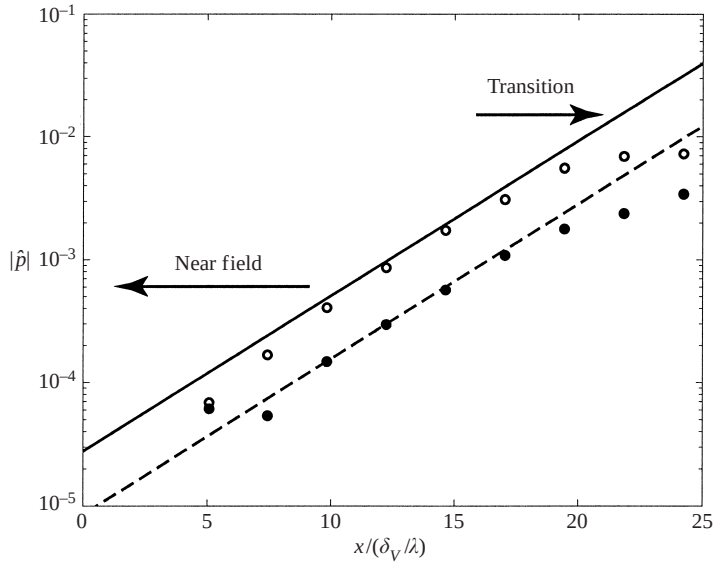

FIGURE 23. Pressure amplitude profiles of instability waves for different source position cases. The absolute values of the pressure fluctuation at the centreline ($y = 0$) are plotted. The DNS data were processed during $t \in [3.0, 4.0)$. Theoretical predictions: ——, $\eta = 0.$; – – –, $\eta = -0.20$ ($\times\delta_V/\lambda$). DNS results: ○, $\eta = 0$. (Case D); ●, $\eta = -0.20$ ($\times\ \delta_V/\lambda$) (Case E).

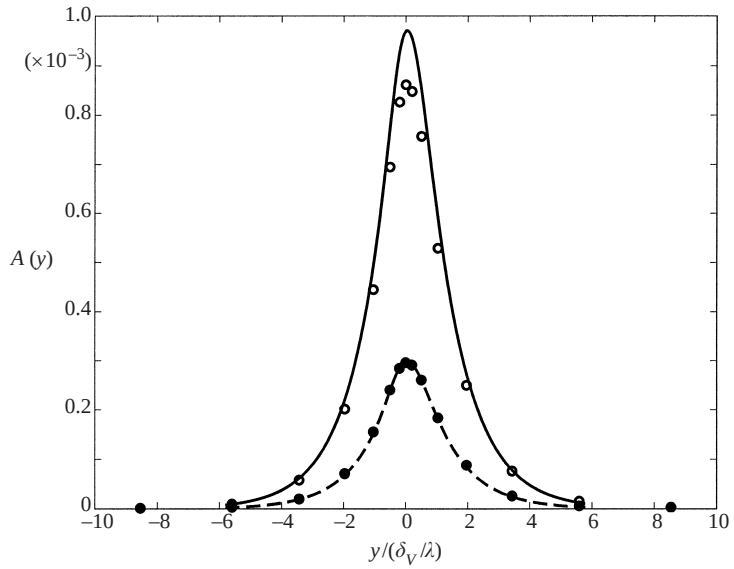

FIGURE 24. Eigenmode shapes of instability waves for different source position cases. The absolute values of the pressure fluctuation at $x = 12.24$ ($\times\delta_V/\lambda$) are plotted. Notation is the same as figure 23.

is reduced to about one-third. Thus, the receptivity is very sensitive to the source position in the inviscid limit. In fact, the characteristics of the adjoint eigenmode shape are fairly close to figure 8 of Balsa (1988). He calculated the receptivity for a piecewise-constant velocity profile and found an asymmetric mode shape; however, this approach requires taking an inverse Fourier transform at each source location.

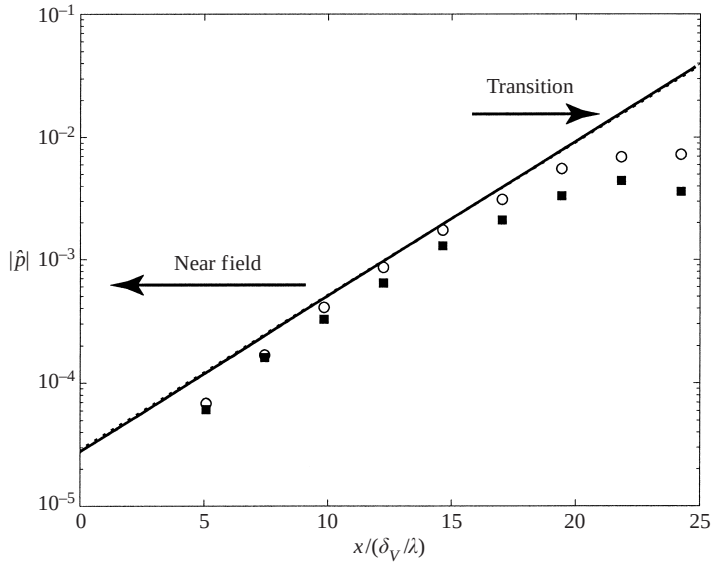

FIGURE 25. Pressure amplitude profiles of instability waves at different Reynolds numbers. The absolute values of the pressure fluctuation at the centreline ($y = 0$) are plotted. The DNS data were processed during $t \in [3.0, 4.0)$. Theoretical predictions: ——, $Re = 10^5$; · · · · · ·, $Re = 2.5 \times 10^3$ (they almost overlap, the deviation is due to different spreading rates). DNS results: ○, $Re = 10^5$ (Case D); ■, $Re = 2.5 \times 10^3$ (Case F).

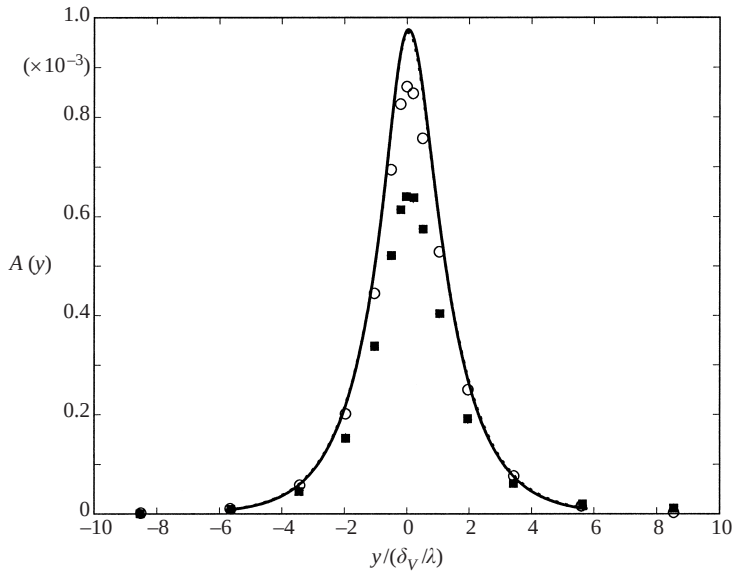

FIGURE 26. Eigenmode shapes of instability waves at different Reynolds numbers. The absolute values of the pressure fluctuation at $x = 12.24$ ($\times \delta_V/\lambda$) are plotted. Notation is the same as figure 25.

Similarly, figures 25 and 26 compare the inviscid theory and the DNS results at two different Reynolds numbers. As described before, the viscous effect should broaden the sharp peak of the adjoint eigenmode shape. In fact, these two figures demonstrate that the growth rate and the eigenmode shape are preserved, but the magnitude in the lower Reynolds number case ($Re = 2.5 \times 10^3$, Case F) is considerably lower than

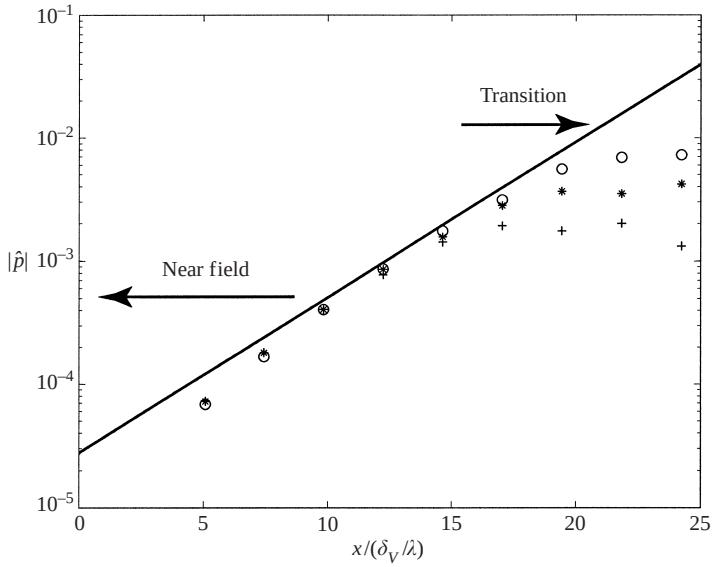

FIGURE 27. Pressure amplitude profiles of instability waves in different time intervals. The absolute values of the pressure fluctuation at the centreline ($y = 0$) are plotted: ——, theoretical prediction; the DNS results (Case D), +, $t \in [2.25, 3.25)$; *, $t \in [2.625, 3.625)$; and ○, $t \in [3.0, 4.0)$.

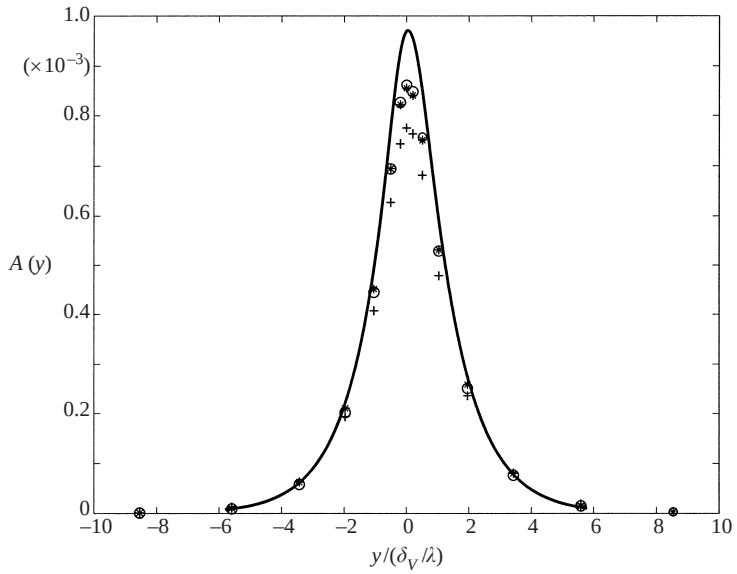

FIGURE 28. Eigenmode shapes of instability waves in different time intervals. The absolute values of the pressure fluctuation at $x = 12.24$ ($\times\delta_V/\lambda$) are plotted. Notation is the same as figure 27.

(by about 70%) the theoretical prediction, as expected. It should be noted that sound wave responses, direct waves and refracted arrival waves, are less sensitive to the Reynolds number.

Strictly speaking, the numerical simulations presented here may require some further grid refinements. A mixing layer at the Reynolds number of $O(10^5)$ produces very intense vortices with strong braid regions in between them. The resolution in the

current DNS might be insufficient to resolve these regions. Therefore, the pressure amplitude profiles were taken during time intervals before the instability waves reached the end of the computational domain. Figures 27 and 28 show the magnitudes of instability waves and their eigenmode shapes processed during different time intervals. This time evolution of growing instability waves confirms that the DNS results at $x = 12.24 \times \delta_V/\lambda$ (at which the eigenmode shapes were plotted) are sufficiently close to the converged solutions.

5. Conclusions

In this study, three types of waves – direct waves, refracted arrival waves, and instability waves – generated by a time-harmonic point source in an isothermal transversely sheared mixing layer are analytically formulated, and these theoretical predictions are compared with DNS at various frequencies.

For the direct waves, the derivation of the low- and high-frequency asymptotic Green's functions are revisited. It is found that the high-frequency Green's function agrees reasonably well with the DNS in all the cases although the low frequency case ($\lambda/\delta_V = 4.0$) in DNS indicates some features predicted in the low-frequency limit. Therefore, one can expect that the high-frequency limit is generally more applicable to estimate the sound pressure levels for broad-band jet noise. To realize the radiation pattern of the low-frequency limit, the forcing frequency needs to be further decreased.

Similarly, for refracted arrival waves the low- and high-frequency asymptotic Green's functions are derived, and they are compared with DNS. The DNS results at different frequencies are found to follow the corresponding frequency limits. This analysis confirms that plane-wave-type sound can propagate in the zone of silence even in subsonic flows; however, the amplitude of these waves is quite sensitive to the velocity profile.

In addition, a method to predict instability waves is developed for the receptivity problem. To determine the magnitude, the normal mode decomposition is used with the adjoint convective wave operator and the corresponding inner product. In the comparison with DNS, the magnitude, the growth rate, and the eigenmode shapes are all well-predicted in the inviscid limit. The shape of the adjoint eigenfunction indicates that the receptivity is fairly sensitive to the source position and the Reynolds number, which is verified using DNS. This approach helps analyse the disturbance levels of instability waves under different conditions of mixing flows.

It should be mentioned that the analyses of this paper are based on laminar parallel mixing layer profiles. However, the asymptotic formulas of low- and high-frequency direct waves are independent of the mean velocity profile in the vertical direction as long as the free-stream velocities are the same. Therefore, the formulas derived here are expected to be valid even for turbulent velocity profiles as long as the turbulent length scale is sufficiently smaller than the acoustic wavelength and the mean flow field can be reasonably approximated as a parallel flow. Of course, in regions where the mean velocity profiles are significantly distorted, such as the end of the potential core of jets, the parallel mean flow assumption fails. Moreover, when the acoustic wavelength is comparable to the turbulent length scales, such as the eddy scale, significant sound scattering should occur. These effects are ignored in the present analyses. For instability waves, the location of the peak in an adjoint eigenmode shape could be fairly sensitive to the velocity profile. On the other hand, the mean velocity profiles of turbulent mixing layers are often reasonably well fitted by a simple analytic function. Studies aiming to elucidate the effects of shear-layer

spreading and scattering associated with turbulence would require simulations of more realistic turbulent flows, which are computationally more demanding. Nonetheless, the present work should be of interest in studies of aero-acoustic problems involving mixing layers and jet flows.

The authors would like to thank Professor Joseph B. Keller for many useful suggestions. We gratefully acknowledge that this research was supported by NASA Ames Research Center (grant number NCC-255 and NAG 2-1373). Computer time for T90 was provided by the National Partnership for Advanced Computational Infrastructure (NPACI) at the San Diego Super Computer Center (SDSC).

Appendix A. Derivation for the low-frequency limit

To derive the solution in the low-frequency limit (2.5), an asymptotic matching is used, which is actually analogous to the vortex sheet approximation. In the inner region, the coefficient of the second term of (2.4), $\bar{n}'/\bar{n}$, becomes $O(1/\epsilon)$, and $\hat{G}''$, $\hat{G}'$, and $\hat{G}$ may become $O(1/\epsilon^2)$, $O(1/\epsilon)$, and $O(1)$, or smaller than these, respectively (as seen later, because the jump condition for $\hat{G}$ does not allow a discontinuity for monopole sources, $\hat{G}''$ and $\hat{G}'$ are actually $O(1/\epsilon)$ and $O(1)$, respectively). From this order analysis, in the region $-\epsilon < y < \eta_-$ and $\eta_+ < y < +\epsilon$, (2.4) can be approximated by

$$\frac{\partial^2 \hat{G}_{(1)}}{\partial y^2} - 2\frac{\bar{n}'}{\bar{n}}\frac{\partial \hat{G}_{(1)}}{\partial y} = \bar{n}^2 \frac{\partial}{\partial y}\left(\frac{1}{\bar{n}^2}\frac{\partial \hat{G}_{(1)}}{\partial y}\right) = 0. \tag{A 1}$$

Therefore, the quantity $(1/\bar{n}^2)(\partial \hat{G}_{(1)}/\partial y)$ is constant in the inner region, except across the source position, $y = \eta$. Accordingly, the derivative conditions in the inner region become

$$\left.\frac{1}{\bar{n}_{-\epsilon}{}^2}\frac{\partial \hat{G}_{(1)}}{\partial y}\right|_{-\epsilon} = \left.\frac{1}{\bar{n}_{\eta}{}^2}\frac{\partial \hat{G}_{(1)}}{\partial y}\right|_{\eta_-}, \tag{A 2}$$

$$\left.\frac{1}{\bar{n}_{+\epsilon}{}^2}\frac{\partial \hat{G}_{(1)}}{\partial y}\right|_{+\epsilon} = \left.\frac{1}{\bar{n}_{\eta}^2}\frac{\partial \hat{G}_{(1)}}{\partial y}\right|_{\eta_+}. \tag{A 3}$$

Here, the subscripts denote the position in the y-coordinate. These relations are simply a vortex sheet (shown in (A 9) and (A 10) later).

To derive the jump conditions across the source position, first integrate (2.4) from η_- to η_+ (take the zeroth-order moment):

$$\int_{\eta_-}^{\eta_+} \bar{n}^2 \frac{\partial}{\partial y}\left(\frac{1}{\bar{n}^2}\frac{\partial \hat{G}_{(1)}}{\partial y}\right) \mathrm{d}y + \int_{\eta_-}^{\eta_+} \omega^2(\bar{n}^2 - \bar{k}^2)\hat{G}_{(1)} \mathrm{d}y = \int_{\eta_-}^{\eta_+} \delta(y-\eta)\,\mathrm{d}y. \tag{A 4}$$

Here, the second term of (A 4) vanishes because it is $O(|\eta_+ - \eta_-|)$, which is essentially zero. Integrating (A 4) by parts yields

$$\left(\left.\frac{\partial \hat{G}_{(1)}}{\partial y}\right|_{\eta+} - \left.\frac{\partial \hat{G}_{(1)}}{\partial y}\right|_{\eta-}\right) - \frac{2\bar{n}'_{\eta}}{\bar{n}_{\eta}}\left(\hat{G}_{(1)}|_{\eta_+} - \hat{G}_{(1)}|_{\eta_-}\right) = 1. \tag{A 5}$$

Next, multiply (2.4) by y and integrate it in the same interval (take the first-order

moment). Integrating it by parts yields

$$\eta\left[\left(\left.\frac{\partial\hat{G}_{(1)}}{\partial y}\right|_{\eta+}+\left.\frac{\partial\hat{G}_{(1)}}{\partial y}\right|_{\eta-}\right)-\frac{2\bar{n}'_{\eta}}{\bar{n}_{\eta}}\left(\hat{G}_{(1)}|_{\eta+}-\hat{G}_{(1)}|_{\eta-}\right)\right]-\left(\hat{G}_{(1)}|_{\eta+}-\hat{G}_{(1)}|_{\eta-}\right)=\eta. \tag{A 6}$$

Combining (A 5) and (A 6), the jump conditions across the source can be obtained as follows:

$$\hat{G}_{(1)}|_{\eta+}-\hat{G}_{(1)}|_{\eta-}=0, \tag{A 7}$$

$$\left.\frac{\partial\hat{G}_{(1)}}{\partial y}\right|_{\eta+}-\left.\frac{\partial\hat{G}_{(1)}}{\partial y}\right|_{\eta-}=1. \tag{A 8}$$

Thus, in the low-frequency limit $\hat{G}_{(1)}(y)$ does not allow discontinuity across the source, but its derivative does. Note that, referring to (A 7) and (A 1), the jump conditions equivalent to a vortex sheet can be expressed as follows:

$$\hat{G}|_2-\hat{G}|_1=0, \tag{A 9}$$

$$\left.\frac{1}{\bar{n}_2^2}\frac{\partial\hat{G}}{\partial y}\right|_2-\left.\frac{1}{\bar{n}_1^2}\frac{\partial\hat{G}}{\partial y}\right|_1=0, \tag{A 10}$$

where the subscripts 1 and 2 denote the lower and the upper sides, respectively.

Now, substituting (A 2) and (A 3) into (A 8) gives

$$\bar{n}_{\eta}^2\left(\left.\frac{1}{\bar{n}_{+\epsilon}^2}\frac{\partial\hat{G}_{(1)}}{\partial y}\right|_{+\epsilon}-\left.\frac{1}{\bar{n}_{-\epsilon}^2}\frac{\partial\hat{G}_{(1)}}{\partial y}\right|_{-\epsilon}\right)=1. \tag{A 11}$$

On the other hand, in the outer region the second term of (2.4) vanishes. Here, specify the velocities in the far fields on both sides as follows: $M(-\infty)=M_1$ and $M(+\infty)=M_2$ (see figure 2). Likewise, define $\bar{n}_1\equiv 1-\bar{k}M_1$ and $\bar{n}_2\equiv 1-\bar{k}M_2$. Consequently, the outer solution can be expressed as follows:

$$\hat{G}_{(1)}(y)\approx\begin{cases}\tilde{\mathscr{A}}_1\exp(-\mathrm{i}\omega\sqrt{\bar{n}_1^2-\bar{k}^2}\;y) & \text{if}\quad y\leqslant-\epsilon,\\ \tilde{\mathscr{A}}_2\exp(\mathrm{i}\omega\sqrt{\bar{n}_2^2-\bar{k}^2}\;y) & \text{if}\quad y\geqslant+\epsilon.\end{cases} \tag{A 12}$$

Note that arbitrary phase variation is included in complex coefficients $\tilde{\mathscr{A}}_J$ $(J=1,2)$, which are $O(1)$. From (A 12), the inner solution must satisfy the following conditions to match the outer solution at $y=\pm\epsilon$:

$$\left.\frac{\partial\hat{G}_{(1)}}{\partial y}\right|_{-\epsilon}=\left.-\mathrm{i}\omega\sqrt{\bar{n}_1^2-\bar{k}^2}\,\hat{G}_{(1)}\right|_{-\epsilon}, \tag{A 13}$$

$$\left.\frac{\partial\hat{G}_{(1)}}{\partial y}\right|_{+\epsilon}=\left.\mathrm{i}\omega\sqrt{\bar{n}_2^2-\bar{k}^2}\,\hat{G}_{(1)}\right|_{+\epsilon}. \tag{A 14}$$

Here, (A 13) and (A 14) show that $\hat{G}|_{-\epsilon}$, $(\partial\hat{G}/\partial y|_{-\epsilon})$, $\hat{G}|_{+\epsilon}$, and $(\partial\hat{G}/\partial y|_{+\epsilon})$ are all $O(1)$. In addition, (A 7) and (A 8) guarantee that $(\partial\hat{G}/\partial y|_{\eta-})$ and $(\partial\hat{G}/\partial y|_{\eta+})$ are also both

$O(1)$. Combining them with (A 11), one can conclude

$$\hat{G}_{(1)}|_{+\epsilon} - \hat{G}_{(1)}|_{-\epsilon} = O(\epsilon). \tag{A 15}$$

Hence, (A 15) gives $\tilde{\mathscr{A}}_1 = \tilde{\mathscr{A}}_2$ in (A 12) at the leading order. Knowing this and combining (A 11), (A 13) and (A 14), one can derive the solution in the low-frequency limit (2.5).

Appendix B. Critical angles in the low- and high-frequency limits

As discussed in §§ 2.1 and 2.2, the amplitudes of both low- and high-frequency limits become peaked when one of the terms in the denominator vanishes. In the low-frequency limit this occurs when $(\bar{n}_J^\star)^2 - (\bar{k}^\star)^2 = 0$ (J takes 1 or 2 on the upper or the lower side, respectively) in two dimensions, while in the high-frequency limit it occurs when $(\bar{n}_\eta^\star)^2 - (\bar{k}^\star)^2 = 0$. Using (2.8), the peak angle can be calculated as

$$\phi_J^{peak} = \mp \arcsin\left[\sqrt{\frac{1 - F(M_J, \bar{k}^\star)}{1 - M_J^2 F(M_J, \bar{k}^\star)}}\right], \tag{B 1}$$

where

$$F(M_J, \bar{k}^\star) = [(1 - M_J^2)\bar{k}^\star + M_J]^2, \tag{B 2}$$

and it is assumed the velocity at the source position is equal to or smaller than the faster free-stream velocity ($\max(M_1, M_2)$). Here, in the low-frequency limit $\bar{k}^\star = 1/(M_2 - 1)$ on the lower side and $\bar{k}^\star = 1/(M_1 + 1)$ on the upper side, while in the high-frequency limit $\bar{k}^\star = 1/(M_\eta \mp 1)$, on the lower and upper sides, respectively.

Appendix C. Jump conditions in the high-frequency limit

To derive the solution (2.15), Goldstein (1982) applied the method developed by Avila & Keller (1963) to the transformed third-order convective wave equation (2.14). This derivation is reviewed here. Start with (2.14) in the high-frequency limit as

$$\frac{\partial^2 \hat{G}^\bullet_{(1)}}{\partial y^2} + \omega^2[\bar{n}^2(y) - \bar{k}^2]\hat{G}^\bullet_{(1)} = \frac{\delta(y - \eta)}{\bar{n}}. \tag{C 1}$$

Assuming the form of the solution to be $\hat{G}^{\bullet,high}_{(1)}(y) \equiv A(y)\mathrm{e}^{\mathrm{i}\omega r\varphi(y)}$, substitute it into (C 1). The leading terms of ω yields

$$\varphi'(y) = \pm\sqrt{\bar{n}^2(y) - \bar{k}^2}. \tag{C 2}$$

Likewise, the second leading terms consist of

$$\mathrm{i}\omega[2\varphi'(y)A'(y) + \varphi''(y)A(y)] = \frac{\delta(y - \eta)}{\bar{n}_\eta}. \tag{C 3}$$

Now, expand the amplitude part as $A(y) \sim \sum_{j=0}^{\infty} A_j(y)/(\mathrm{i}\omega)^j$ with $A_0(y) \equiv 0$. After some calculation, the leading term of (C 3) becomes

$$(\varphi'(y)A_1^2(y))' = \frac{A_1(\eta)\delta(y - \eta)}{\bar{n}_\eta}. \tag{C 4}$$

Therefore, two jump conditions across the source can be obtained from (C 2) and (C 4) as follows:

$$[\varphi'(\eta)]_{y=\eta_-}^{\eta_+} = 2\sqrt{\bar{n}_\eta^2 - \bar{k}^2}, \tag{C 5}$$

$$[\varphi'(\eta)]_{y=\eta_-}^{\eta_+} A_1(\eta) = \frac{1}{\bar{n}_\eta}. \tag{C 6}$$

Combining (C 5) and (C 6), the amplitude at the source position can be calculated as

$$A_1(\eta) = \frac{1}{2\bar{n}_\eta\sqrt{\bar{n}_\eta^2 - \bar{k}^2}}. \tag{C 7}$$

Furthermore, (C 4) indicates that $(\varphi' A_1^2)$ is conserved, except at the source position. Hence, the amplitude of the outer solution becomes

$$A_1(y) = \frac{(\bar{n}_\eta^2 - \bar{k}^2)^{1/4}}{(\bar{n}^2(y) - \bar{k}^2)^{1/4}} A_1(\eta). \tag{C 8}$$

Substituting (C 2), (C 7) and (C 8) into the original geometrical expansion, the asymptotic solution for $\hat{G}_{(1)}^{high}$ yields (2.15) since $\hat{G}_{(1)}^{\bullet} = \hat{G}_{(1)}/\bar{n}(y)$.

REFERENCES

Ahluwalia, D. S. & Keller, J. B. 1977 Exact and asymptotic representations of the sound field in a stratified ocean. In *Wave Propagation and Underwater Acoustics* (ed. J. B. Keller & J. S. Papadakis). Lecture Notes in Physics, vol. 70, pp. 14–84. Springer.

Atvars, J., Schubert, L. K. & Ribner, H. S. 1965 Refraction of sound from a point source placed in an air jet. *J. Acoust. Soc. Am.* **37**, 168–170.

Avila, G. S. S. & Keller, J. B. 1963 The high-frequency asymptotic field of a point source in an inhomogeneous medium. *Commun. Pure Appl. Maths* **16**, 363–381.

Balsa, T. F. 1976 The far field of high-frequency convected singularities in sheared flows, with an application to jet-noise prediction. *J. Fluid Mech.* **74**, 193–208.

Balsa, T. F. 1977 The acoustic field of sources in shear flow with application to jet noise: convective amplification. *J. Fluid Mech.* **74**, 33–47.

Balsa, T. F. 1988 On the receptivity of free shear layers to two-dimensional external excitation. *J. Fluid Mech.* **187**, 155–177.

Balsa, T. F. 1989 Three-dimensional wave packets and instability waves in free shear layers and their receptivity. *J. Fluid Mech.* **201**, 77–97.

Beckemeyer, R. J. 1974 Application of an inner expansion method of plane, inviscid, compressible flow stability studies. *J. Fluid Mech.* **62**, 405–416.

Blokhintzev, D. I. 1946 The propagation of sound in an inhomogeneous and moving medium I. *J. Acoust. Soc. Am.* **18**, 322–328.

Durbin, P. A. 1983*a* High frequency Green's function for aerodynamic noise in moving media, Part I: General theory. *J. Sound Vib.* **91**, 519–525.

Durbin, P. A. 1983*b* High frequency Green's function for aerodynamic noise in moving media, Part II: Noise from a spreading jet. *J. Sound Vib.* **91**, 527–538.

Freund, J. B. 1997 Proposed inflow/outflow boundary condition for direct computation of aerodynamic sound. *AIAA J.* **35**, 740–742.

Friedland, A. B. & Pierce, A. D. 1969 Reflection of acoustic pulse from stable and instable interfaces between moving fluids. *Phys. Fluids* **12**, 1148–1159.

Giles, M. B. 1990 Nonreflecting boundary conditions for Euler equation calculations. *AIAA J.* **28**, 2050–2058.

Goldstein, M. E. 1975 The low frequency sound from multipole sources in axisymmetric shear flows, with applications to jet noise. *J. Fluid Mech.* **70**, 595–604.

GOLDSTEIN, M. E. 1976 The low frequency sound from multipole sources in axisymmetric shear flows. Part 2. *J. Fluid Mech.* **75**, 17–28.

GOLDSTEIN, M. E. 1978 Characteristics of the unsteady motion on transversely sheared mean flows. *J. Fluid Mech.* **84**, 305–329.

GOLDSTEIN, M. E. 1982 High frequency sound emission from moving point multipole sources embedded in arbitrary transversely sheared mean flows. *J. Sound Vib.* **80**, 499–522.

HOWE, M. S. 1970 Transmission of an acoustic pulse through plane vortex sheet. *J. Fluid Mech.* **43**, 353–367.

KELLER, J. B. & LEWIS, R. M. 1995 Asymptotic methods for partial differential equations: The reduced wave equation and Maxwell's equations. In *Survey in Applied Mathematics* (ed. J. B. Keller, D. W. McLaughlin & G. C. Papanicolaou), vol. 1, pp. 1–28. Plenum Press.

KHAVARAN, A. & KREJSA, E. A. 1994 Refraction of high frequency noise in an arbitrary jet flow. *AIAA Paper* 94-0139.

LANDAU, L. D. & LIFSHITZ, E. M. 1987 *Fluid Mechanics*, 2nd Edn, pp. 276–281. Pergamon.

LELE, S. K. 1992 Compact finite difference schemes with spectral-like resolution. *J. Comput. Phys.* **103**, 16–42.

LIGHTHILL, M. J. 1952 On sound generated aerodynamically: I. General theory. *Proc. R. Soc. Lond.* A **211**, 564–587.

LILLEY, G. M. 1974 On the noise from jet. *AGARD CP* 131, pp. 1–12.

LUSH, P. A. 1971 Measurements of subsonic jet noise and comparison with theory. *J. Fluid Mech.* **46**, 477–500.

MANI, R. 1976*a* The influence of jet flow on jet noise. Part 1. The noise of unheated jets. *J. Fluid Mech.* **73**, 753–778.

MANI, R. 1976*b* The influence of jet flow on jet noise. Part 2. The noise of heated jets. *J. Fluid Mech.* **73**, 779–793.

PIERCE, A. D. 1989 *Acoustics: An Introduction to Its Physical Principles and Applications.* The Acoustic Society of America.

PRIDMORE-BROWN, D. C. 1958 Sound propagation in a fluid flowing through an attenuating duct. *J. Fluid Mech.* **4**, 393–406.

SALWEN, H. &. GROSCH, C. E. 1981 The continuous spectrum of the Orr–Sommerfeld equation. Part 2. Eigenfunction expansions. *J. Fluid Mech.* **104**, 445–465.

SUZUKI, T. 2001 Acoustic wave propagation in transversely sheared flows. PhD thesis, Stanford University, Stanford.

SUZUKI, T. & LELE, S. K. 2002 Refracted arrival waves in a zone of silence from a finite thickness mixing layer. *J. Acoust. Soc. Am.* **111**, 716–728.

SUZUKI, T. & LELE, S. K. 2003 Green's functions for a source in a boundary layer: direct waves channelled waves and diffracted waves. *J. Fluid Mech.* **477**, 129–173 (referred to herein as Part 2).

TAM, C. K. W. 1978 Excitation of instability waves in a two-dimensional shear layer by sound. *J. Fluid Mech.* **89**, 357–371.

TAM, C. K. W. & AURIAULT, L. 1998 Mean flow refraction effects on sound radiated from localized sources in a jet. *J. Fluid Mech.* **370**, 149–174.

TAM, C. K. W. & BURTON, D. E. 1984 Sound generated by instability waves of supersonic flows. Part 1. Two-dimensional mixing layer. *J. Fluid Mech.* **138**, 249–271.

TANNA, H. K. 1977 An experimental study of jet noise. Part I: Turbulent mixing noise. *J. Sound Vib.* **50**, 405–428.

TESTER, B. J. & MORFEY, C. L. 1976 Developments in jet noise modelling – theoretical predictions and comparisons with measured data. *J. Sound Vib.* **46**, 79–103.